

---

# Training-Free Generation of Protein Sequences from Small Family Alignments via Stochastic Attention

---

Jeffrey D. Varner

R.F. Smith School of Chemical and Biomolecular Engineering  
Cornell University, Ithaca, NY 14850  
jdv27@cornell.edu

## Abstract

Generating novel protein sequences that respect the statistical constraints of a family typically requires training deep generative models on thousands to millions of examples. Yet most protein families are small: the median Pfam family has fewer than 100 members, a regime where learned models overfit or collapse. We propose *stochastic attention* (SA), a training-free sampler that treats the modern Hopfield energy over a set of stored protein sequences as a Boltzmann distribution and draws samples via Langevin dynamics. The score function is given in closed form by the residual of a single softmax attention operation, eliminating the need for a trained score network, external pretraining data, or graphics processing unit (GPU) resources. Each iteration costs  $\mathcal{O}(dK)$ , where  $d$  is the sequence representation dimension and  $K$  is the number of stored family members (two matrix-vector products). Across eight Pfam families ( $K=37\text{--}420$  sequences,  $L=23\text{--}262$  residues), including candidate antimicrobial beta defensins, SA generates sequences with low amino acid Kullback–Leibler (KL) composition divergence ( $\text{KL}\leq 0.06$ ), substantial novelty (0.40–0.65), and structural plausibility confirmed by ESMFold and AlphaFold2 (mean predicted local distance difference test [pLDDT] up to 95). Generated sequences achieve significantly higher template modeling scores (TM-scores) to canonical family folds than natural family members in six of eight families tested by ESMFold ( $p < 0.05$ ), a result corroborated by AlphaFold2 cross-validation across all eight families. Head-to-head comparison with profile hidden Markov models (HMMs), EvoDiff, and the multiple sequence alignment (MSA) Transformer shows that learned baselines produce sequences that drift far from the family (as low as 11% sequence identity), while SA maintains 51–66% identity, staying within the functional envelope while remaining novel. Stochastic attention achieves this in seconds on a laptop, compared to hours of GPU or CPU time for pretrained alternatives, and scales stably down to  $K=20$  sequences. A consensus-with-noise control and a column-permuted alignment control confirm that SA captures covariance structure beyond marginal frequencies, and leave-one-family-out cross-validation of the  $\beta^*$  predictor ( $R^2 > 0.90$ ) confirms out-of-sample generalization. Independent validation by ESM2-650M confirms that generated sequences are recognized as comparably protein-like to natural family members, and cross-referencing against published deep mutational scanning experiments shows that over 90% of SA-generated substitutions correspond to experimentally tolerated mutations. The critical inverse temperature  $\beta^*$  governing the generation–retrieval transition is predicted from principal component analysis (PCA) dimensionality alone ( $R^2=0.97$ ), enabling fully automatic operation from a seed alignment.

**Significance Statement.** Most protein families have fewer than 100 known members, too few to train a deep generative model. We show that a single attention operation over a family alignment defines an energy landscape whose Boltzmann distribution can be sampled exactly via Langevin dynamics, with no training, no GPU, and no external data. The resulting method, stochastic attention, generates novel protein sequences that preserve family-level amino acid statistics and are predicted by independent structure predictors to adopt the correct fold across eight diverse protein families, including candidate antimicrobial peptides. A simple linear relationship between the dimensionality of the sequence representation and the critical sampling temperature enables fully automatic operation from a seed alignment, opening training-free sequence generation to most protein families that are too small for conventional deep learning.

## 1 Introduction

With protein structure prediction largely solved by AlphaFold2 [1] and RoseTTAFold [2], the frontier has shifted toward the inverse problem: *designing* novel protein sequences with desired properties [3, 4]. Generative approaches now span a broad landscape, from classical profile hidden Markov models (pHMMs) [5, 6] that capture single-site statistics, to Potts models and direct coupling analysis (DCA) [7–9] that capture pairwise epistasis, to deep generative models including variational autoencoders [10–12], large autoregressive language models [13–15], alignment-processing transformers [16], MSA-conditioned diffusion [17], and structure-conditioned methods such as ProteinMPNN [18] and RFdiffusion [19]. These structure-based methods are powerful when a target backbone is available but do not address the problem we consider: generating novel sequences from a family alignment alone.

All of the sequence-level approaches above share a common requirement: large training corpora. Language models are pretrained on millions of UniRef50 sequences; even MSA-conditioned methods require either extensive pretraining or large input alignments. This reliance on scale creates a fundamental blind spot. The median Pfam family contains fewer than 100 full-length members [20], and thousands of families have fewer than 50. The long tail of protein space, orphan families, newly discovered clades from metagenomic surveys, and engineered libraries from directed evolution, may have only a handful of characterized sequences. In this scarce-data regime, learned generative models face a parameter-to-data ratio problem: deep models overfit and collapse in diversity, while pHMMs emit sequences that drift far from the family’s functional envelope. Yet these small families are precisely where generative tools could have the greatest impact [21]. What is needed is an approach that can extract the statistical structure of a protein family from whatever data is available, even a few dozen sequences, without learning parameters that could overfit.

A separate line of work provides this capability, by revealing that the attention mechanism at the heart of modern transformers [22] is itself an energy-based model. Ramsauer et al. [23] showed that a single softmax attention operation is equivalent to one step of the retrieval dynamics on the modern Hopfield energy with a log-sum-exp interaction function, building on the dense associative memory framework of Krotov and Hopfield [24], which itself generalized the classical Hopfield network [25] to continuous states and exponential storage capacity beyond the  $0.14N$  limit established for binary networks [26]. This connection endows any set of stored examples with a well-defined energy landscape: the examples become memory patterns, the energy is minimized at (and near) those patterns, and the Boltzmann distribution over this landscape assigns high probability to states that resemble the stored set. Concurrently, score-based generative models [27, 28] and denoising diffusion models [29] have demonstrated that samples can be drawn from complex distributions by estimating the score function  $\nabla \log p(\mathbf{x})$  and running Langevin dynamics [30]. These methods achieve state-of-the-art sample quality in images, molecules, and protein structures, but they require a trained neural network to approximate the score. The Energy Transformer [31] exploits the Hopfield energy for discriminative tasks but does not sample from the associated Boltzmann distribution. The key insight we build on is that the Hopfield energy provides the score function *analytically*, as the residual of a single attention operation, which means that Langevin sampling can proceed without learning any parameters at all.

We propose an approach to protein sequence generation that requires no training. We observe that the modern Hopfield energy over a set of stored protein sequences defines a Boltzmann distribution whose score function is given in closed form by the residual of a single attention operation:  $\nabla \log p_\beta(\xi) = \beta(\mathbf{T}(\xi) - \xi)$ , where  $p_\beta$  is the Boltzmann density at inverse temperature  $\beta$ ,  $\xi$  is the query state, and

**T** is the softmax attention map. Because the score is exact, there is no score-estimation error, and the sampler inherits the convergence guarantees of the unadjusted Langevin algorithm (ULA) [32, 33]. Langevin dynamics on this energy yields a training-free sampler that we call *stochastic attention*: each iteration performs a softmax-weighted pull toward stored family members, a contraction toward the origin, and an isotropic Gaussian perturbation, requiring only two matrix-vector products per step ( $\mathcal{O}(dK)$  cost, no GPU, no backpropagation). The inverse temperature  $\beta$  controls the balance between exploration and retrieval: at low  $\beta$  the sampler explores broadly, generating novel sequences that blend features from multiple stored patterns; at high  $\beta$  it retrieves sequences close to individual memories. Our prior work [34] introduced stochastic attention and validated it on synthetic data, MNIST digits, financial time series, and a single protein family (RRM). The present work makes the following protein-specific contributions beyond the original method paper: (i) systematic validation across eight diverse Pfam families spanning a ten-fold range of family sizes; (ii) structure-level validation using two independent predictors (ESMFold and AlphaFold2); (iii) an empirical scaling law for the critical temperature ( $\beta^* \approx 1.57 + 0.28\sqrt{d}$ ,  $R^2=0.97$ ) with out-of-sample cross-validation; (iv) a scaling study demonstrating robustness down to  $K=20$  sequences; (v) head-to-head comparison against four protein-specific baselines (profile HMMs, EvoDiff, MSA Transformer, Potts model); (vi) pairwise mutual information analysis showing that SA captures correlational structure beyond marginal frequencies; (vii) independent validation by ESM2-650M and deep mutational scanning cross-referencing; and (viii) consensus-with-noise and column-permuted alignment controls that distinguish SA from a consensus generator.

The key question this paper addresses is: *what can you generate from a small protein family alignment with no training?* Across eight Pfam families spanning a ten-fold range of family sizes ( $K=37-420$ ) and a seven-fold range of sequence lengths ( $L=23-262$ ), we show that stochastic attention produces novel sequences that preserve family-level amino acid composition ( $KL < 0.06$ ) and achieve substantial novelty (0.40–0.65 in PCA space), while being predicted to fold into the correct three-dimensional architecture by both ESMFold [35] and AlphaFold2 [1], as assessed by TM-align [36] structural comparison. We characterize the critical inverse temperature  $\beta^*$  at which the sampler transitions from diffuse exploration to pattern retrieval, and show that  $\beta^*$  can be predicted from PCA dimensionality alone ( $R^2=0.97$ ), enabling fully automatic operation from a seed alignment. A systematic scaling study reveals stable generation quality down to  $K=20$  sequences, the regime where learned models struggle most. Head-to-head comparison with profile HMMs [5], EvoDiff [17], and the MSA Transformer [16] reveals that stochastic attention balances compositional fidelity, sequence novelty, and structural viability without external training data. Independent validation by ESM2-650M [35] confirms that generated sequences are recognized as protein-like by a language model trained on billions of evolutionary sequences, and cross-referencing against published deep mutational scanning data [37, 38] shows that over 90% of SA-generated substitutions correspond to experimentally tolerated mutations.

## 2 Results

We ran stochastic attention on all eight Pfam families (Table 1) and observed that the method consistently generated novel protein sequences while preserving family-level amino acid statistics, across a ten-fold range of family sizes and a seven-fold range of sequence lengths (Fig. 1; SI Appendix, Table S2).

We first examined whether the sampler converged to the correct Boltzmann distribution by comparing the outputs of the unadjusted Langevin algorithm (ULA) and its Metropolis-adjusted variant (MALA; see Materials and Methods). The MALA acceptance rates exceeded 99.6% in every family tested (range: 99.6%–99.8%), confirming that the ULA discretization bias was negligible at step size  $\alpha=0.01$ . The two samplers produced near-identical metrics: for example, in the RRM family, SA retrieval achieved novelty 0.243 and KL divergence 0.107, while MALA yielded 0.249 and 0.112, respectively. This agreement held across all eight families, which justified the use of the computationally cheaper ULA in subsequent experiments.

We next assessed amino acid composition fidelity across families. In the generation regime (inverse temperature  $\beta \approx 2\beta^*$ , just above the entropy inflection point where pattern-specific basins first emerge; see Materials and Methods), stochastic attention (SA) achieved Kullback–Leibler (KL) divergences (lower indicates better compositional fidelity) below 0.06 in every family, with several families below 0.02 (SI Appendix, Table S2). For comparison, bootstrap KL divergences ranged more

widely (0.007–0.133) across families, reflecting the finite-sample variance of uniformly resampling a small stored set: SA outperformed bootstrap in six of eight families, with the two exceptions (SH3 and zf-C2H2, bootstrap KL 0.030 and 0.007) occurring in families where the stored set was large enough that uniform resampling already produced a representative composition estimate. The convex combination baseline performed poorly (KL=0.06–2.35), confirming that averaging across stored patterns destroyed the peaked, position-specific residue distributions characteristic of conserved protein families (SI Appendix, Fig. S1).

We then examined whether the generated sequences were novel or replaying stored patterns. In the generation regime, novelty (higher indicates greater departure from stored patterns) ranged from 0.40 (Defensin\_beta) to 0.65 (WW), indicating substantial departure from any single stored memory (SI Appendix, Table S2). The generated ensembles also exhibited high diversity: mean pairwise cosine distance was  $\approx 1.0$  in every family (0.998–1.001), confirming that the sampler produced distinct, well-separated sequences rather than repeatedly generating the same or nearly identical outputs (mode collapse). By contrast, bootstrap samples had zero novelty by construction, and Gaussian perturbation produced negligible novelty ( $< 0.02$  in all families), confirming that small additive noise is insufficient to escape the basin of the nearest stored pattern. The retrieval regime produced intermediate novelty (0.17–0.35), consistent with samples that explore locally around stored patterns without fully escaping their basins. Nearest sequence identity to a stored pattern (where values near the within-family range indicate generation within the functional envelope, while very high values suggest memorization and very low values suggest drift outside the family) confirmed this picture: generation-regime sequences had 51–66% identity to the nearest stored sequence, comparable to the typical within-family identity, while retrieval-regime sequences remained at 53–85% identity depending on the family’s intrinsic diversity.

We next turned to the scaling study, in which we subsampled the WW domain at  $K \in \{20, 50, 100, 200, 400\}$  with five independent replicates per condition to characterize how generation quality, latent dimensionality, and the critical temperature co-vary with family size (SI Appendix, Fig. S2). Stochastic attention in the generation regime maintained low KL divergence across the entire range: KL=0.019  $\pm$  0.008 at  $K=20$ , improving monotonically to KL=0.010  $\pm$  0.002 at  $K=400$ . This gradual degradation contrasted sharply with the convex combination baseline, whose KL divergence exceeded 0.8 at every family size and worsened with increasing  $K$  (0.81 at  $K=20$  to 1.50 at  $K=400$ ), confirming that averaging over more patterns compounds the smoothing artifact. Bootstrap and Gaussian perturbation maintained moderate KL values (0.02–0.03) but produced no novelty at any  $K$ , making them ineffective as generative methods. The PCA dimensionality grew with family size, from  $d=17$ –18 components at  $K=20$  to  $d=182$ –183 at  $K=400$ , and the critical temperature tracked this growth ( $\beta^*=2.7$  to 5.5). Despite the six-fold increase in effective dimensionality, SA generation quality remained stable, which suggested that the entropy inflection criterion successfully adapted the operating temperature to the geometry of the memory matrix at each scale. Novelty increased with  $K$  (from 0.47 at  $K=20$  to 0.74 at  $K=400$ ), reflecting the richer landscape of a larger memory set, while nearest sequence identity decreased correspondingly (from 0.71 to 0.56), indicating that the sampler explored further from stored patterns when more patterns were available to collectively shape the energy landscape.

The scaling study revealed that  $\beta^*$  tracks PCA dimensionality; we next characterized this relationship across the full set of eight families. The empirical  $\beta^*$  ranged from 3.2 (PDZ, Pkinase) to 5.4 (WW), consistently lower than the  $\sqrt{d}$  prediction for random patterns (where  $d$  is the principal component analysis [PCA] dimension retaining 95% of alignment variance) (5.8–13.6). The ratio  $\beta^*/\sqrt{d}$  was approximately 0.4–0.6 across all families, which indicated that the structured similarity spectrum of real protein sequences, arising from conserved positions, correlated substitutions, and phylogenetic signal, shifts the retrieval-to-generation transition to lower temperatures. Families with higher mean per-column Shannon entropy ( $\bar{H}_{\text{col}}$ , measured in nats) tended to have lower  $\beta^*/\sqrt{d}$  ratios, consistent with the intuition that more diverse families require less thermal energy to escape stored patterns. The effective number of sequences  $K_{\text{eff}}$ , computed by reweighting sequences at 80% identity to down-weight near-duplicates, equaled  $K$  in all but the WW family ( $K_{\text{eff}}=419$  vs.  $K=420$ ), indicating minimal redundancy in the Pfam seed alignments.

Given this consistent relationship, we asked whether the critical temperature could be predicted from alignment statistics alone, without running an explicit temperature sweep (Fig. 2). We pooled 33 data points (the 8 Pfam families and 25 WW scaling replicates) and regressed  $\beta^*$  against MSA-derived

features. We found that a simple two-parameter model,  $\beta^* \approx 1.57 + 0.28\sqrt{d}$  (intercept  $1.57 \pm 0.07$ , slope  $0.281 \pm 0.007$ ;  $\pm$  denotes bootstrap standard error [SE], 10,000 resamples), explained 97% of the variance ( $R^2=0.97$ , root-mean-square error [RMSE]=0.16), with  $d$  the PCA dimension at 95% retained variance. Adding further predictors (mean column entropy  $H_{\text{col}}$ , effective number of sequences  $K_{\text{eff}}$ , or spectral concentration  $\lambda_1/\text{tr}(\mathbf{C})$ , the fraction of total variance explained by the leading principal component) produced negligible improvement ( $\Delta R^2 < 0.001$ ; the physically motivated bifurcation predictor  $\beta_c = 1/\lambda_1(\mathbf{C})$  achieved only  $r=0.48$ , SI Appendix, Fig. S9), which indicated that PCA dimensionality captured most of the relevant variation. The fitted slope of 0.28 was roughly half the  $\sqrt{d}$  coefficient predicted for random patterns, consistent with the empirical ratio  $\beta^*/\sqrt{d} \approx 0.4\text{--}0.6$  observed across families. The naive random-pattern prediction  $\beta^* = \sqrt{d}$  yielded RMSE=5.3, a  $33\times$  larger error, confirming that the structured similarity spectrum of real protein families shifts the phase transition to substantially lower temperatures. Refitting the model on the eight Pfam families alone (excluding WW scaling replicates, which contribute 25 of the 33 points) yielded a nearly identical relationship ( $\beta^* = 1.64 + 0.278\sqrt{d}$ ,  $R^2=0.95$ ), confirming that the result is not driven by overrepresentation of a single family (Appendix S15). This regression provides a practical shortcut: given a new family, one can estimate  $\beta^*$  from PCA alone and set the generation temperature without a temperature sweep.

We compared stochastic attention against three established learned baselines – profile HMM emit, EvoDiff (MSA-conditioned diffusion), and the MSA Transformer (Gibbs masked language model sampling) – across all eight families (Fig. 3), using Wilcoxon rank-sum tests on per-chain estimates (30 chains  $\times$  5 samples) with Cohen’s  $d$  effect sizes. EvoDiff and profile HMM emit achieved the lowest KL divergences (EvoDiff: 0.003–0.011 in the seven shorter families; HMM: 0.006–0.031), consistent with their direct access to pretraining data or position-specific frequencies. Stochastic attention generation was competitive (0.008–0.060) despite using only the family’s seed alignment with no external training data. EvoDiff’s performance degraded sharply on the longest family: for Pkinase ( $L=262$ ), EvoDiff produced KL=0.20, an order of magnitude worse than SA (0.04), and required  $\sim 14$  hours on CPU compared to seconds for SA (SI Appendix, Table S9).

The three metrics together revealed a trade-off that no single learned baseline resolved (Fig. 3). Profile HMM emit and the MSA Transformer produced sequences with high novelty but low identity to stored patterns (11–59%), indicating sequences that have drifted outside the family’s characteristic sequence space. EvoDiff produced intermediate sequence identity (0.15–0.57) but still significantly lower than SA generation in every family ( $p < 0.001$ ). Stochastic attention occupied the regime of low KL divergence, substantial novelty (0.40–0.65), and moderate sequence identity (51–66%), generating sequences that departed meaningfully from stored patterns while remaining within the family. SA achieved this balance without pretraining, backpropagation, or GPU resources. As a further comparison, we fitted a Potts model via pseudo-likelihood maximization (plmDCA) to two families and generated sequences by Gibbs sampling (SI Appendix, Table S5). The Potts model, which captures pairwise coevolutionary couplings with approximately 500,000 fitted parameters, achieved comparable composition fidelity and novelty to SA, but with slightly lower sequence identity to stored patterns. The similar output quality suggests that the information captured by pairwise couplings is also implicitly encoded in the Hopfield energy landscape; the critical difference is that SA requires no parameter fitting and runs in seconds rather than minutes.

We assessed structural plausibility by predicting folded structures for 50 sequences per method per family using ESMFold (Fig. 4), comparing SA generation to stored (natural) sequences via Wilcoxon rank-sum tests with Cohen’s  $d$  effect sizes. We used two complementary metrics: the predicted local distance difference test (pLDDT), a per-residue folding confidence score where values above 70 indicate a confident prediction, and the template modeling score (TM-score), a global measure of structural similarity where values above 0.5 indicate the same fold. Throughout this section and the baseline comparison, we report both raw  $p$ -values and note that all reported significant results ( $p < 0.05$ ) survive Benjamini-Hochberg false discovery rate correction at  $q=0.05$  across the approximately 40 statistical tests performed across families and metrics.

SA-generated sequences achieved mean pLDDT scores statistically indistinguishable from stored natural sequences in six of eight families (Wilcoxon  $p > 0.05$ ), with significantly *higher* pLDDT in Kunitz (90.8 vs. 89.3,  $p=0.001$ ,  $d=0.67$ ). Only SH3 showed lower pLDDT for SA generation (70.5 vs. 74.1,  $p=0.006$ ), though the mean remained above the confidence threshold; as described below, this deficit was not confirmed by AlphaFold2 cross-validation. Across all families,  $\geq 86\%$  of SA-generated sequences exceeded pLDDT=70. TM-scores showed a consistent pattern: in six

of eight families, SA generation achieved significantly *higher* TM-scores than stored sequences ( $p < 0.05$ ;  $d > 1.0$  in RRM, WW, PDZ, and Pkinase; Fig. 4). This likely reflects the Boltzmann ensemble’s tendency to weight the central tendency of the family distribution, producing sequences closer to a “consensus fold” than individual natural sequences, which carry lineage-specific structural deviations.

As an independent cross-validation, we repeated the structure prediction for all eight families using AlphaFold2 (AF2) (Fig. 5; SI Appendix, Fig. S3). The AF2 results corroborated the ESMFold findings across all eight families while resolving the single negative result: for SH3, the only family where ESMFold had indicated a significant pLDDT deficit, AlphaFold2 showed no pLDDT difference ( $p=0.99$ ) and significantly higher TM-scores for SA generation (0.736 vs. 0.721,  $p < 0.001$ ). The pattern was consistent across the remaining seven families: pLDDT was statistically indistinguishable from stored sequences in four of seven (RRM: 80.9 vs. 79.2,  $p=0.17$ ; Kunitz: 94.9 vs. 93.3,  $p=0.18$ ; PDZ: 84.6 vs. 82.6,  $p=0.81$ ; Defensin\_beta: 84.7 vs. 84.1,  $p=0.09$ ), with WW and zf-C2H2 showing significantly higher pLDDT for SA generation (WW: 84.7 vs. 83.1,  $p=0.005$ ,  $d=0.55$ ; zf-C2H2: 92.8 vs. 89.2,  $p < 0.001$ ,  $d=0.52$ ). Pkinase was the only family where SA generation showed significantly lower pLDDT (86.2 vs. 88.9,  $p < 0.001$ ,  $d=-0.90$ ), though both means remained well above the confidence threshold of 70. Despite this pLDDT deficit, Pkinase SA-generated sequences achieved significantly higher TM-scores (0.702 vs. 0.671,  $p < 0.001$ ,  $d=1.42$ ), consistent with the consensus-fold effect. TM-scores were significantly higher for SA generation in all eight families ( $p < 0.05$ ; Cohen’s  $d=0.47-1.73$ ). The PDZ family showed the largest effect, with SA generation achieving TM-scores of 0.638 vs. 0.559 for stored sequences ( $p < 0.001$ ,  $d=1.52$ ). The concordance between two independent structure predictors across all eight families strengthens the computational evidence that SA-generated sequences are predicted to adopt the correct fold (SI Appendix, Fig. S4; TM-score concordance  $r=0.999$ ). To complement the aggregate statistics, we selected the highest-confidence SA-generated structure from each family and superimposed it on the experimentally determined reference structure, confirming sub-angstrom predicted backbone RMSD despite 40–65% novelty relative to all stored family members.

To understand how SA-generated sequences achieve structural fidelity while maintaining high novelty, we examined the position-specific substitution pattern of the Kunitz domain in detail (Fig. 6). We aligned the five highest-confidence SA-generated sequences (AlphaFold2 pLDDT  $\geq 96$ ) against the family consensus and colored each position by its conservation level in the stored MSA. All five sequences preserved every highly conserved position (11 of 11 positions with  $> 90\%$  conservation) and all six cysteines that form the three disulfide bonds defining the Kunitz fold, while introducing 17–25 amino acid substitutions concentrated at evolutionarily variable positions. No substitutions occurred at the structural glycines (positions 9, 34, 37) that enable tight turns, or at the phenylalanine and asparagine residues (positions 30, 38, 40, 42) that anchor the hydrophobic core. The per-position Shannon entropy of SA-generated sequences correlated strongly with that of the stored MSA ( $r=0.968$ ), confirming that the Boltzmann sampling procedure recapitulates the position-specific conservation landscape of the family. Positions that are constrained by structure or function in natural sequences remain invariant in the generated ensemble, while positions that tolerate variation in nature exhibit comparable diversity in the generated output. This selectivity arises without any explicit conservation mask or position-specific prior: it emerges naturally from the energy landscape defined by the stored patterns, in which conserved positions create deep, narrow wells that the sampler cannot escape, while variable positions define broad, shallow basins that permit exploration.

The preceding analysis established that SA preserves the single-site conservation landscape of each family. We next asked whether this fidelity extends to pairwise residue covariation, which reflects structural contacts and functional couplings that single-site statistics cannot capture. We computed pairwise mutual information (MI) matrices for the stored and SA-generated alignments in each family and correlated the  $L(L-1)/2$  upper-triangle MI values (SI Appendix, Fig. S6, Table S6). Across seven of the eight families, the Pearson correlation between stored and SA-generated MI vectors ranged from  $r=0.53$  to 0.92 (mean  $r=0.72$  excluding Pkinase), confirming that SA-generated sequences preserve the pairwise coupling landscape of their parent family. The strongest MI preservation occurred in families with large  $K$  relative to  $L$  (zf-C2H2:  $r=0.92$ ; Defensin\_beta:  $r=0.85$ ), while the lowest occurred in Pkinase ( $r=0.05$ ), where only 37 sequences span 262 alignment positions, a regime in which MI estimation is unreliable for any method. Notably, SA generation substantially outperformed profile HMMs in every family (e.g., Kunitz:  $r=0.80$  vs. 0.32; WW:  $r=0.71$  vs. 0.29), which confirmed that the Hopfield energy captures correlational structure beyond

what position-independent models encode. As expected, methods that explicitly model pairwise couplings (Potts/plmDCA:  $r=0.75-0.89$  in SH3 and Kunitz) or that leverage millions of pretraining MSAs (EvoDiff:  $r=0.59-0.97$ ) achieved higher MI correlations than SA, which fits no parameters and uses only the seed alignment. For three families where the reference PDB structure closely matched the alignment length (Kunitz, SH3, Defensin\_beta), we mapped structural contacts ( $C\alpha-C\alpha$  distance  $<8 \text{ \AA}$ , sequence separation  $\geq 5$ ) to alignment positions and found that MI at contact pairs in the SA-generated ensemble tracked MI at those same pairs in the stored alignment ( $r=0.49-0.86$ ; SI Appendix, Fig. S6), confirming that covariation preservation extends to structurally relevant positions.

As a complementary, sequence-level assessment of biological plausibility, we scored all SA-generated and stored sequences using ESM2-650M [35], a protein language model pretrained on millions of UniRef50 sequences that is entirely independent of the stochastic attention framework (SI Appendix, Table S3). We computed pseudo-perplexity via masked marginal scoring, where lower values indicate a more protein-like sequence. SA-generated sequences were statistically indistinguishable from natural family members in four of eight families (Wilcoxon  $p > 0.05$ ; RRM, zf-C2H2, Pkinase, Defensin\_beta), with SA achieving significantly better scores in the Kunitz domain (4.47 vs. 4.98,  $p < 0.001$ ,  $d=-0.74$ ). Three families showed modestly higher pseudo-perplexity for SA generation (SH3, WW, PDZ;  $d=0.6-1.0$ ), though all SA-generated sequences remained well within the range of natural protein sequences (overall mean: 5.71 vs. 5.58). This independent validation confirms that SA-generated sequences are recognized as protein-like by a language model trained on billions of evolutionary sequences. We further cross-referenced SA-generated substitutions against published deep mutational scanning (DMS) datasets for the PDZ domain (McLaughlin et al. [37]) and the SH3 domain (Faure et al. [38]), finding that 91.7% and 90.4% of matched substitutions, respectively, corresponded to experimentally tolerated mutations, significantly exceeding the baseline tolerance rates of 77.5% and 67.5% in the DMS datasets (binomial  $p < 10^{-135}$  and  $p < 10^{-156}$ ; SI Appendix, Table S4). The continuous DMS fitness scores of SA-generated substitutions were also significantly higher than those of random single mutations (Cohen's  $d=0.42$  and 0.70), confirming that the Boltzmann sampling procedure preferentially generates substitutions that have been experimentally validated as functional.

The beta defensin family (PF00711) provided an opportunity to test whether SA generation preserves not only sequence-level statistics but also the biophysical properties that underpin antimicrobial function (Fig. 7). Beta defensins are short cationic peptides whose antimicrobial activity [39] depends on a conserved six-cysteine disulfide scaffold, net positive charge at physiological pH, and moderate hydrophobicity. We computed net charge (at pH 7, counting K and R as +1, D and E as -1, H as +0.5), hydrophobic residue fraction, and cysteine count for all stored, SA-generated, and baseline sequences. SA-generated sequences preserved the six-cysteine scaffold ( $6.01 \pm 0.08$  mean cysteines, compared to  $6.02 \pm 0.15$  for natural sequences), maintained a cationic charge profile ( $+6.1 \pm 1.6$  vs.  $+5.2$  for stored sequences) with the narrowest charge distribution of any method, and occupied the same region of charge-hydrophobicity space as natural defensins. We defined a minimal antimicrobial plausibility filter requiring net charge  $\geq +2$ , hydrophobic fraction between 0.3 and 0.7, and at least four cysteines. By this criterion, 51% of SA-generated sequences passed, compared to 42% of stored sequences, 53% for EvoDiff, 25% of HMM-emitted sequences, and 16% of MSA Transformer sequences. EvoDiff achieved a comparable pass rate but required hours of GPU compute and millions of pretraining sequences. We emphasize that passing this coarse biophysical filter does not imply antimicrobial activity; whether SA-generated defensins fold correctly, form the required disulfide bonds in vitro, or exhibit membrane-disrupting function are open experimental questions.

### 3 Discussion

We set out to ask what can be generated from a small protein family alignment with no training. The answer: sequences that are novel, compositionally faithful, and predicted by independent structure predictors to adopt the correct three-dimensional fold, produced in seconds on a laptop from nothing but the alignment itself. Across eight Pfam families spanning a ten-fold range of family sizes ( $K=37-420$ ) and a seven-fold range of sequence lengths ( $L=23-262$ ), stochastic attention produced output quality comparable to methods pretrained on millions of sequences, while requiring zero external data, zero training, and zero GPU resources. The generated sequences preserved family-level amino acid composition ( $KL < 0.06$ ), achieved substantial novelty (0.40-0.65), and were predicted by ESMFold and AlphaFold2 to adopt the correct three-dimensional fold. This combination of properties was not

achieved by any single learned baseline we tested: profile HMMs and the MSA Transformer generate sequences that drift outside the family, EvoDiff requires millions of pretraining sequences and hours of compute, and all three sacrifice sequence identity to stored patterns in ways that stochastic attention does not. The fact that a training-free method, one that treats the seed alignment as both the model and the data, produces output comparable to systems built on orders of magnitude more information suggests that the statistical structure of protein families is rich enough to support generation without learned representations, provided the generative framework respects the geometry of the family’s sequence space.

The structure validation results were noteworthy. SA-generated sequences achieved significantly higher TM-scores to the canonical family fold in six of eight families by ESMFold (Wilcoxon  $p < 0.05$ ). This was not an artifact of sequence similarity: the same generated sequences had 40–65% novelty relative to stored patterns. Two (non-exclusive) explanations are possible, but the predictor-bias explanation is likely the primary factor. Structure predictors (ESMFold, AlphaFold2) are trained on evolutionary data and may assign higher confidence to sequences that resemble a family’s central tendency, inflating TM-scores for consensus-proximal inputs regardless of true structural quality. Since the Boltzmann ensemble defined by the Hopfield energy weights the central tendency of the family distribution, the generated sequences are inherently closer to consensus than individual natural sequences (which carry lineage-specific structural deviations), making them particularly susceptible to this bias. An alternative explanation is that the consensus-proximal sequences genuinely adopt a fold closer to the canonical family structure. The fact that both predictors agree is consistent with either interpretation, since both are trained on the same evolutionary data. A definitive resolution would require experimental structure determination of selected generated sequences. The pLDDT confidence scores told a complementary story: SA-generated sequences were statistically indistinguishable from stored sequences in six of eight families by ESMFold ( $p > 0.05$ ), confirming that the sampler does not sacrifice folding confidence for diversity. The single exception, SH3, where ESMFold reported a modest pLDDT deficit (70.5 vs. 74.1), was resolved by AlphaFold2 cross-validation, which showed no pLDDT difference (90.7 vs. 89.3,  $p=0.99$ ) and significantly higher TM-scores for SA generation (0.736 vs. 0.721,  $p < 0.001$ ). The concordance between two independent structure predictors across all eight families, and the resolution of the only negative result as a predictor-specific artifact, is consistent with the conclusion that SA-generated sequences are predicted to adopt the correct fold, though we emphasize that both predictors are neural models trained on evolutionary data and experimental structure determination of selected generated sequences would provide definitive confirmation.

A broader methodological caveat applies to all computational validation in this study. Both structure predictors (ESMFold, AlphaFold2), the protein language model (ESM2-650M), and the DMS fitness assays are all trained on, or derived from, evolutionary sequence data. High scores for sequences that resemble natural family members are therefore expected, and the validation is inherently circular: we generate sequences from an alignment, then evaluate them with tools trained on similar alignments. The consensus-with-noise and column-permuted alignment controls (Appendix S18, S19) provide evidence that SA captures structure beyond marginal frequencies, and the near-duplicate analysis (Appendix S17) confirms that generated sequences are not trivially close to stored patterns, but these controls do not break the circularity of the structure prediction validation. We therefore frame the structure prediction results as “consistent with foldability” rather than proof of correct folding; experimental structure determination remains the gold standard.

Comparison against three established baselines (profile HMM emit, EvoDiff, and the MSA Transformer) revealed a trade-off that stochastic attention resolves differently from any single learned baseline. All three baselines produced sequences with significantly lower identity to stored family members than SA generation ( $p < 0.001$  in every family, with effect sizes  $d = 1.1$ – $26.8$ ). Profile HMM emit and the MSA Transformer generated sequences at 9–59% identity, well below the typical within-family range, suggesting sequences that had drifted outside the family’s functional envelope. EvoDiff balanced the metrics more effectively in shorter families but required pretraining on millions of UniRef50 MSAs, scaled poorly with sequence length (~14 hours for 150 Pkinase sequences on CPU, compared to 0.2–4.6 s for SA across all families; Appendix S12), and suffered a sharp degradation in compositional fidelity on the longest family (Pkinase KL=0.20, an order of magnitude worse than SA). Stochastic attention occupied the middle ground (low KL divergence, high novelty, moderate sequence identity) using only the seed alignment. We note that each baseline was designed for a different use case and optimized for different objectives. The lower sequence identity of HMM

emit and the MSA Transformer may reflect intentional exploration of broader sequence space rather than poor quality, and the low identity may be desirable for applications seeking maximally diverse functional sequences. Additionally, EvoDiff and MSA Transformer runtimes were measured on CPU; with GPU acceleration (the intended deployment), both methods would run substantially faster than the CPU times reported here. A targeted comparison with a Potts model fitted via pseudo-likelihood maximization (plmDCA) on two families (SI Appendix, Table S5) revealed that pairwise coevolutionary models achieved comparable output quality to SA, despite fitting approximately 500,000 parameters to fewer than 100 sequences. This convergence is informative: it suggests that the modern Hopfield energy, through the softmax attention operation, implicitly captures the same correlational structure that Potts models fit explicitly, but without parameter estimation. The pairwise mutual information analysis (SI Appendix, Table S6) provides direct evidence for this implicit coupling: SA-generated sequences preserved the pairwise MI landscape of the stored alignment (Pearson  $r=0.53-0.92$  across seven families), consistently exceeding the MI preservation of profile HMMs ( $r=0.07-0.83$ ), which model each position independently. That SA captures substantial pairwise structure without fitting any parameters is consistent with the exponential storage capacity of modern Hopfield networks, in which the softmax attention operation couples all positions simultaneously through the stored-pattern energy landscape. Methods that fit pairwise couplings explicitly (Potts) or draw on large-scale pretraining (EvoDiff) achieve stronger MI preservation, reflecting their direct access to pairwise or higher-order statistics; the relevant comparison for SA, however, is against single-site models, where the improvement demonstrates that the Hopfield energy encodes information beyond marginal frequencies. The practical advantage is that SA avoids the fitting step entirely, which becomes increasingly fragile as the data-to-parameter ratio falls below  $10^{-4}$ , a regime that encompasses most Pfam families. This makes the method well suited to orphan families, newly discovered protein clades, or engineered libraries where external training corpora are unavailable or inappropriate.

The beta defensin results (Fig. 7) illustrate a broader principle: the Boltzmann ensemble over a family alignment implicitly enforces the biophysical constraints characteristic of the family, without any explicit objective for charge, hydrophobicity, or disulfide topology. This implicit enforcement arises because the energy landscape concentrates probability near the stored patterns, which already satisfy these constraints by virtue of being functional proteins. The preservation of the six-cysteine scaffold and cationic charge profile is encouraging, but the biophysical filter used here is coarse: only 42% of natural stored defensin sequences pass the same filter, indicating a 58% false-negative rate on known functional sequences. This filter therefore assesses consistency with stored biophysical properties rather than plausibility for antimicrobial function, and compositional consistency does not imply biological activity. Wet-lab characterization of selected generated sequences would be needed to validate the method's utility for therapeutic peptide design.

The scaling study on the WW domain showed that this balance is not fragile: stochastic attention maintained stable generation quality down to  $K=20$  sequences, with KL divergence below 0.02 and novelty above 0.47 even at this extreme. This robustness arises from a structural property of the method: the energy landscape is defined entirely by the stored patterns, with no parameters that could overfit to a small training set. There is no encoder to memorize, no decoder to collapse, and no denoising network to undertrain. The entropy inflection criterion automatically adapts the operating temperature to the geometry of the memory matrix at each scale, and the critical temperature  $\beta^*$  itself can be predicted from PCA dimensionality alone ( $R^2=0.97$ ), eliminating the need for a temperature sweep and enabling fully automatic operation from a seed alignment. In contrast, learned generative models face a fundamental parameter-to-data ratio problem when  $K < 100$ : VAEs and diffusion models have thousands to millions of parameters that cannot be meaningfully constrained by a few dozen sequences, and even the most parameter-efficient approaches (e.g., profile HMMs) emit sequences that lack the higher-order correlations needed for structural integrity. This regime,  $K < 100$ , encompasses most Pfam families and the long tail of protein space where generative tools are most needed.

Several limitations should be acknowledged. The most significant is that stochastic attention operates on a fixed alignment representation: it requires a pre-computed MSA and a fixed alignment length  $L$ , and cannot generate insertions, deletions, or variable-length sequences. This constraint is inherited from the one-hot-plus-PCA encoding, which maps each sequence to a vector of fixed dimension  $20L$ ; any change in  $L$  would alter the representation space itself. In practice, this means that the method is best suited to compact, well-aligned domains rather than multi-domain proteins or families

with frequent large insertions. Extending stochastic attention to variable-length generation would likely require replacing PCA with a length-agnostic embedding (e.g., learned or kernel-based) while preserving the closed-form score function, a nontrivial but tractable direction for future work. The PCA projection discards information that may be relevant for capturing higher-order correlations, and the choice of retained variance (95%) involves a trade-off between compactness and expressiveness. A systematic sensitivity analysis spanning 50%–99% retained variance across all eight families revealed that generation quality is robust throughout the 75%–99% range, with KL divergence, novelty, and sequence identity varying by less than 0.04, 0.16, and 0.10, respectively (Appendix S13). Below approximately 70% retained variance, compositional fidelity began to degrade in the most diverse families (WW: KL rising from 0.03 to 0.15; RRM: from 0.06 to 0.19), while compact families (PDZ, Pkinase, Defensin\_beta) remained stable even at 50%. The transition threshold is governed by the alignment’s spectral structure: families whose eigenvalue spectrum decays slowly require more principal components to encode position-specific variation. The practical floor of ~70–75% retained variance provides a useful guideline, and the 95% default lies well within the robust regime. The primary scaling study used WW domain subsamples; to test generality, we replicated the  $K=20$  condition on three additional families (SH3, Kunitz, zf-C2H2), finding consistent generation quality across all four (KL < 0.03, novelty  $\approx 0.47$ ; Appendix S3). The multi-chain initialization strategy initializes chains near stored patterns for computational convenience, but this choice is not critical: replacing stored-pattern initialization with random points on the unit sphere produced indistinguishable output across all eight families, confirming that the burn-in period is sufficient to reach stationarity from any starting point (Appendix S11). The multi-chain protocol does not, however, guarantee coverage of all modes in the Boltzmann distribution, particularly for very large or highly diverse families. The eight families studied here are all well-structured, globular domains with abundant structural and functional annotation; this choice was necessary for validation (structure prediction, DMS cross-referencing, biophysical analysis) but introduced a selection bias toward precisely the class of proteins that structure predictors handle best. Performance on intrinsically disordered regions, transmembrane domains, multi-domain proteins, or families with very low sequence identity remains untested. The method’s reliance on PCA may be particularly limiting for disordered families, where sequence variation is less structured and the low-dimensional projection may not capture the relevant degrees of freedom. Finally, our structure validation used ESMFold and AlphaFold2, which are themselves neural models with biases; wet-lab characterization of selected generated sequences would provide stronger evidence of functional viability and is a natural next step.

Looking beyond proteins, the connection between attention and Boltzmann sampling suggests a broader principle: any set of examples, regardless of domain, defines an energy landscape via the modern Hopfield energy, and Langevin dynamics on this landscape provides a principled generative model with no training. The requirements are minimal: the examples must be representable as vectors in a common space, and the practitioner must choose an inverse temperature that balances fidelity and diversity. This perspective may extend naturally to other biological sequence families where data is scarce but examples are structured, such as antibody repertoires (where individual clonotypes may have only a handful of somatic variants), RNA families (where Rfam seed alignments are typically smaller than their Pfam counterparts), or small-molecule libraries (where chemical series may contain only tens of analogs). Beyond biology, any domain with a small, curated set of high-quality examples, such as materials compositions, musical motifs, or architectural floor plans, could in principle benefit from the same framework. The analytic score function also provides a natural interface with the convergence theory of Langevin dynamics [32, 33], enabling formal guarantees on sample quality that are absent from most neural generative models, and opening a path toward certifiable generation in safety-critical applications such as therapeutic protein design.

As a future direction, directed generation of binding proteins is a natural extension of the current framework. Binding specificity is relational, depending on both the generated protein and a particular target, and the family alignment encodes the fold and general functional constraints but not target-specific information. However, the same Langevin sampling machinery could in principle be conditioned on target-relevant subsets by curating the memory matrix with experimentally characterized binders. This “small-set amplifier” use case is well matched to the method’s strengths in the small-family regime, though we emphasize that the current work does not demonstrate or validate this capability. Whether SA-generated sequences would preserve binding function, as opposed to fold and composition, remains an open experimental question.

In summary, stochastic attention is a training-free alternative to learned generative models for protein sequence generation, particularly suited to the small-family regime that characterizes most of protein space. The method requires only a seed alignment, has  $\mathcal{O}(dK)$  per-step cost, needs no GPU, and produces sequences that are predicted to be structurally plausible and whose diversity and composition match those of natural family members. Experimental characterization of selected generated sequences would be the natural next step to validate these computational predictions and establish the method’s utility for protein engineering applications.

## 4 Materials and Methods

### 4.1 From Hopfield Energy to Score Function

Let  $\mathbf{X} = [\mathbf{m}_1, \dots, \mathbf{m}_K] \in \mathbb{R}^{d \times K}$  be the memory matrix whose columns are vectorized protein sequences from a family alignment of  $K$  members, each represented in  $d$  dimensions (after encoding and, optionally, PCA projection). The modern Hopfield energy [23] is given by:

$$E(\boldsymbol{\xi}) = \frac{1}{2} \|\boldsymbol{\xi}\|^2 - \frac{1}{\beta} \log \sum_{k=1}^K \exp(\beta \mathbf{m}_k^\top \boldsymbol{\xi}), \quad (1)$$

where  $\beta > 0$  is an inverse temperature. The gradient is  $\nabla E(\boldsymbol{\xi}) = \boldsymbol{\xi} - \mathbf{T}(\boldsymbol{\xi})$ , where

$$\mathbf{T}(\boldsymbol{\xi}) := \mathbf{X} \operatorname{softmax}(\beta \mathbf{X}^\top \boldsymbol{\xi}) \quad (2)$$

is the softmax attention retrieval map [23]. The Boltzmann distribution [40]  $p_\beta(\boldsymbol{\xi}) \propto \exp(-\beta E(\boldsymbol{\xi}))$  has score function given by:

$$\nabla \log p_\beta(\boldsymbol{\xi}) = -\beta \nabla E(\boldsymbol{\xi}) = \beta(\mathbf{T}(\boldsymbol{\xi}) - \boldsymbol{\xi}). \quad (3)$$

This score is *exact* and computed by a single attention operation; no score network or training is required.

Applying the unadjusted Langevin algorithm (ULA) [41] to the potential  $U = \beta E$  with step size  $\tilde{\alpha} = \alpha/\beta$  yields the *stochastic attention* update:

$$\boldsymbol{\xi}_{t+1} = (1 - \alpha) \boldsymbol{\xi}_t + \alpha \mathbf{X} \operatorname{softmax}(\beta \mathbf{X}^\top \boldsymbol{\xi}_t) + \sqrt{\frac{2\alpha}{\beta}} \boldsymbol{\epsilon}_t, \quad \boldsymbol{\epsilon}_t \sim \mathcal{N}(\mathbf{0}, \mathbf{I}) \quad (4)$$

Each step performs three operations: (i) contraction toward the origin, (ii) a softmax-weighted pull toward stored memories, and (iii) isotropic Gaussian noise scaled by  $\sqrt{2\alpha/\beta}$ . The per-step cost is  $\mathcal{O}(dK)$ : two matrix-vector products and one softmax. As  $\beta \rightarrow \infty$  the noise vanishes and the update reduces to deterministic retrieval; as  $\beta \rightarrow 0$  sampling becomes noise-dominated.

### 4.2 Critical Temperature from PCA Dimensionality

The attention entropy  $H(\beta) = -\sum_k p_k \log p_k$ , where  $p_k = \operatorname{softmax}(\beta \mathbf{X}^\top \boldsymbol{\xi})_k$ , quantifies selectivity:  $H = \log K$  when attention is uniform ( $\beta \rightarrow 0$ ) and  $H \rightarrow 0$  when attention concentrates on a single memory ( $\beta \rightarrow \infty$ ). The entropy derivative satisfies [34]:

$$\frac{dH}{d\beta} = -\beta \operatorname{Var}_{\mathbf{p}}(e), \quad (5)$$

where  $e_k = \mathbf{m}_k^\top \boldsymbol{\xi}$  are the query-memory similarities. The maximum rate of entropy loss occurs at the inflection point  $\beta^*$  satisfying  $d^2 H/d\beta^2 = 0$ , which marks the onset of pattern-specific structure in the energy landscape. The form of  $\beta^*$  is constrained by the geometry of the stored patterns. Because the memory columns lie on the unit sphere  $\mathbb{S}^{d-1}$ , concentration of measure dictates that the similarity variance is  $\operatorname{Var}(e_k) = 1/d$  exactly for any query drawn uniformly from  $\mathbb{S}^{d-1}$  (Appendix S15). The characteristic similarity scale is therefore  $\sigma = 1/\sqrt{d}$ , and since  $\beta$  enters the softmax as  $\beta e_k$ , the inflection must occur when  $\beta\sigma = \mathcal{O}(1)$ , giving  $\beta^* \sim \sqrt{d}$ . A separate calculation shows that the softmax entropy over  $K$  i.i.d. Gaussian scores undergoes its inflection at a dimensionless temperature  $\tau^* \approx 1.6$  that is nearly independent of  $K$  for  $K \geq 30$  (Appendix S15), providing a universal baseline for the transition.

Empirically, we find a simple linear relationship across eight Pfam families and WW-domain subsamples spanning  $K = 20\text{--}420$  and  $d = 18\text{--}186$  (Results):

$$\beta^* \approx 1.57 + 0.28\sqrt{d}, \quad (6)$$

which captures 97% of the variance ( $R^2 = 0.97$ , bootstrap median over 10,000 resamples; see Appendix S15 for the full OLS fit and uncertainty analysis). The intercept  $1.57 \approx \tau^*$  recovers the universal softmax inflection baseline, confirming that the same dimensionless transition governs both idealized Gaussian scores and real protein similarities. The coefficient 0.28 of  $\sqrt{d} = 1/\sigma$  is substantially smaller than the pure Gaussian prediction  $\tau^*/\sigma \approx 1.6\sqrt{d}$ ; this reduction arises because  $\beta^*$  is computed at stored patterns  $\mathbf{m}_k$ , where the self-similarity  $\mathbf{m}_k^\top \mathbf{m}_k = 1$  anchors one score at the maximum of  $\mathbb{S}^{d-1}$  and makes concentration easier than for a random query (Appendix S15). From a practical standpoint, Eq. (6) enables fully automatic operation: given a seed alignment,  $d$  is determined by PCA at 95% variance, and  $\beta^*$  follows without a temperature sweep.

### 4.3 Regularity and Convergence

The modern Hopfield energy has Lipschitz-continuous gradient with constant  $L = 1 + \beta\sigma_{\max}^2/2$ , where  $\sigma_{\max} = \|\mathbf{X}\|_{\text{op}}$ , and satisfies the dissipativity condition  $\langle \nabla E(\boldsymbol{\xi}), \boldsymbol{\xi} \rangle \geq \|\boldsymbol{\xi}\|^2/2 - M^2/2$  with  $M = \max_k \|\mathbf{m}_k\|$  [34]. When  $\beta\sigma_{\max}^2 < 2$ , the energy is strictly convex and ULA iterates converge to  $p_\beta$  in Wasserstein-2 distance at a geometric rate [33, 32].

In the protein setting, operating temperatures of interest satisfy  $\beta\sigma_{\max}^2 \gg 2$ , placing the sampler in a non-convex regime where the energy landscape has multiple metastable basins concentrated near the stored patterns. Following standard practice for multimodal Langevin sampling [42], we adopt a multi-chain protocol:  $N_c$  independent chains are initialized near distinct stored patterns, exploiting fast intra-basin mixing while achieving inter-basin coverage through diverse initialization (empirically, random initialization on  $\mathbb{S}^{d-1}$  produces identical output after burn-in; Appendix S11). The Metropolis-adjusted variant (MALA) provides an acceptance-rate diagnostic: acceptance rates near 1.0 confirm that ULA discretization bias is negligible for the chosen step size  $\alpha$ .

We applied stochastic attention to protein sequence generation across eight Pfam families and conducted a systematic scaling study to characterize performance as a function of family size. All experiments used the unadjusted Langevin algorithm (ULA) with step size  $\alpha = 0.01$ . For each family and condition, we ran 30 independent chains of  $T = 5,000$  iterations, initialized near randomly chosen stored patterns with Gaussian perturbation ( $\sigma_{\text{init}} = 0.01$ ). After discarding 2,000 burn-in iterations and thinning every 100 steps, we retained 5 evenly spaced samples per chain for a total of  $S = 150$  generated sequences per condition. The burn-in budget provides a 3–7 $\times$  margin over the empirical convergence point, and the thinning interval matches the integrated autocorrelation time ( $\tau_{\text{int}} \approx 76\text{--}122$  iterations), yielding approximately independent samples (Appendix S10). Metropolis-adjusted Langevin algorithm (MALA) chains were run in parallel with identical parameters to provide acceptance-rate diagnostics; acceptance rates of 99.6–99.8% confirmed that ULA discretization bias is negligible at this step size. Throughout, we used PCA dimensionality reduction retaining 95% of the variance in the one-hot encoded alignment, followed by unit-norm projection to form the memory matrix  $\hat{\mathbf{X}}$ . A sensitivity analysis confirmed that generation quality is robust across the 75%–99% range, with a practical floor near 70% retained variance (Appendix S13). The complete pipeline, from seed alignment to decoded amino acid sequences, is summarized in Algorithm 1 (SI Appendix).

The inverse temperature was set automatically for each family via the entropy inflection criterion described above. We identified  $\beta^*$  from the attention entropy curve and operated in two regimes, both above  $\beta^*$ . Below  $\beta^*$  the energy landscape is essentially flat and Langevin dynamics degenerates into a random walk on the sphere, producing sequences with no family-specific structure. Above  $\beta^*$ , metastable basins form around stored patterns and the sampler begins to produce protein-like sequences. We therefore defined a *generation* regime at  $\beta_{\text{gen}} \approx 2\beta^*$ , just above the transition, where the basins are shallow enough that the sampler can hop between them, producing novel recombinations of family features. At much higher inverse temperature, we defined a *retrieval* regime at  $\beta_{\text{ret}} \approx 20\beta^*$ , where the basins are deep and each chain remains trapped near its initialization pattern, producing near-copies of stored sequences. Three simple baselines were evaluated under identical conditions: bootstrap replay (uniform resampling of stored patterns), Gaussian perturbation (stored pattern plus isotropic noise matched to the SA noise scale), and random convex combination (Dirichlet-weighted average of all stored patterns).

We evaluated generated sequences using five metrics. *Novelty* measured departure from stored patterns as  $1 - \max_k \cos(\hat{\xi}, \mathbf{m}_k)$  in PCA space. *Diversity* quantified the spread of the generated ensemble as the mean pairwise cosine distance among all  $\binom{S}{2}$  pairs of generated samples; a value near 1.0 indicates that generated sequences are uniformly distributed rather than collapsed to a single mode. *Sequence identity* was the maximum fraction of matching residues between a generated sequence and any stored sequence, computed after argmax decoding from PCA space back to amino acid sequences. *KL divergence* of amino acid composition quantified how well generated sequences preserved the family’s residue frequency distribution. *Valid residue fraction* confirmed that all decoded positions were standard amino acids.

**Protein families and scaling study.** We selected eight families spanning a range of sizes, sequence lengths, and conservation levels (Table 1): RRM (PF00076,  $K=68$ ,  $L=71$ ), SH3 (PF00018,  $K=55$ ,  $L=48$ ), WW (PF00397,  $K=420$ ,  $L=31$ ), Kunitz (PF00014,  $K=99$ ,  $L=53$ ), zinc finger C2H2 (PF00096,  $K=151$ ,  $L=23$ ), PDZ (PF00595,  $K=44$ ,  $L=83$ ), protein kinase (PF00069,  $K=37$ ,  $L=262$ ), and beta defensin (PF00711,  $K=45$ ,  $L=36$ ). Seed alignments were downloaded from InterPro [20] and cleaned by removing columns with  $> 50\%$  gaps and sequences with  $> 30\%$  gaps. The resulting PCA dimensions ranged from  $d=34$  (Pkinase) to  $d=186$  (WW). To characterize how generation quality degrades with decreasing family size, we also conducted a scaling study in which we fixed the WW domain (the largest family,  $K=420$ ) and subsampled to  $K \in \{20, 50, 100, 200, 400\}$ . At each value of  $K$  we drew five independent random subsets, rebuilt the memory matrix from scratch (re-computing PCA and  $\beta^*$ ), ran stochastic attention and all baselines, and recorded metrics; this design isolates the effect of family size from family identity, and the five repeats provide error estimates.

**Learned baselines.** To contextualize SA against methods that require pretraining on large external corpora, we compared three established generative approaches for protein sequences. (i) *Profile HMM emit*: we built a profile HMM from each family’s seed alignment using HMMER3 [5] (`hmmbuild -amino`) and emitted  $S=150$  sequences with `hmmemit -N 150 -seed 42`. Emitted sequences were filtered to standard amino acids and truncated or padded to the alignment length  $L$ . (ii) *EvoDiff*: we used the MSA-conditioned order-agnostic discrete diffusion model (MSA\_OA\_DM\_RANDSUB) [17], which was pretrained on UniRef50 MSAs. Generation used the default denoising schedule with MaxHamming subsampling of the conditioning MSA (depth  $\leq 64$ ). (iii) *MSA Transformer*: we used the 100M-parameter MSA Transformer [16] (`esm_msa1b_t12_100M_UR50S`) for generation via iterative Gibbs-like masked language model sampling: a fully masked query row was appended to the family MSA (depth  $\leq 128$ ), and 50 rounds of masking 15% of positions and resampling from the softmax were performed. For each baseline, the same 150-sequence budget and the same evaluation metrics (KL, novelty, sequence identity) were applied. EvoDiff was run on CPU; for the Pkinase family ( $L=262$ ), a single sequence required  $\sim 7$  minutes, yielding  $\sim 14$  hours for 150 sequences (compared to seconds for SA).

**Structure validation.** To assess whether generated sequences adopt structures consistent with their target family, we predicted the three-dimensional structure of 50 sequences per method per family using the ESMFold API [35]. For each predicted structure, we extracted the mean predicted local distance difference test (pLDDT) score from the B-factor column as a measure of folding confidence (pLDDT  $> 70$  indicates a confident prediction). We then compared each predicted structure to a representative experimentally determined structure for the family using TM-align [36] (TM-score  $> 0.5$  indicates the same fold). Reference structures were obtained from the Research Collaboratory for Structural Bioinformatics Protein Data Bank (RCSB PDB): 1FXL (RRM), 1SHG (SH3), 1PIN (WW), 1BPI (Kunitz), 1ZAA (zf-C2H2), 1BE9 (PDZ), 1ATP (Pkinase), and 1E4S (Defensin\_beta). As a positive control, we also predicted structures for 50 stored (natural) sequences from each family, providing an upper bound on expected pLDDT and TM-score. As an independent cross-validation, we repeated the structure prediction for all eight families using AlphaFold2 [1] via ColabFold [43], predicting 50 SA-generated and 50 stored sequences per family with the `alphafold2_ptm` model (single model, 3 recycles, no relaxation). For each family, we selected the SA-generated structure with the highest mean pLDDT and superimposed it on the experimental reference using PyMOL to produce the structural gallery in Fig. 5.

**Antimicrobial peptide biophysical analysis.** The beta defensin family (PF00711) provided an opportunity to assess whether generated sequences preserved biophysical properties associated with

antimicrobial function. For each generated and stored sequence, we computed the net charge at pH 7 (summing +1 for Arg and Lys, -1 for Asp and Glu), the hydrophobic residue fraction (Ala, Val, Ile, Leu, Met, Phe, Trp, Pro), the mean Kyte–Doolittle hydrophobicity, and the cysteine count. We defined an antimicrobial plausibility filter requiring net charge  $\geq +2$ , hydrophobic ratio in  $[0.3, 0.7]$ , and  $\geq 4$  cysteines (reflecting the three disulfide bonds characteristic of the beta-defensin fold), and computed the pass rate for each method.

**Critical temperature prediction.** We pooled  $n=33$  data points (the 8 Pfam families and 25 WW scaling replicates, 5 family sizes  $\times$  5 repeats) and fit ordinary least-squares regression models predicting  $\beta^*$  from MSA-derived features. We considered four candidate features:  $\sqrt{d}$  (PCA dimensionality at 95% retained variance), mean per-column Shannon entropy  $\bar{H}_{\text{col}}$ ,  $\log K_{\text{eff}}$  (effective number of sequences at 80% identity), and spectral concentration  $\lambda_1/\text{tr}(\mathbf{C})$  (leading eigenvalue of the sequence covariance, normalized by trace). We evaluated nested models by adding features in order of marginal  $R^2$  improvement. Uncertainty on regression coefficients was quantified via nonparametric bootstrap: we resampled the 33 observations with replacement 10,000 times, refitting the model on each resample, and reported the standard deviation of the bootstrap distribution as the coefficient SE. Model comparison used root-mean-square error (RMSE) and  $R^2$ , with the naive random-pattern prediction  $\beta^* = \sqrt{d}$  as a reference baseline.

## Acknowledgments

The idea for stochastic attention arose while developing a lecture on energy-based methods for eCornell; preparing that material brought together modern Hopfield networks and Langevin sampling in a way that suggested the framework presented here. We thank the Pfam/InterPro consortium for maintaining publicly available seed alignments. Structure predictions were performed using ESMFold and AlphaFold2 (via ColabFold). Computations were performed on resources at Cornell University.

**Author contributions.** J.D.V. designed research, performed research, analyzed data, and wrote the paper.

**Competing interests.** The author declares no competing interest.

**Data availability.** All code, data, and analysis scripts are available at <https://github.com/varnerlab/SA-Protein-Modeling-Study>. Pfam seed alignments were obtained from InterPro [20]. Reference structures were obtained from the RCSB Protein Data Bank.

## References

- [1] John Jumper, Richard Evans, Alexander Pritzel, Tim Green, Michael Figurnov, Olaf Ronneberger, Kathryn Tunyasuvunakool, Russ Bates, Augustin Žídek, Anna Potapenko, et al. Highly accurate protein structure prediction with AlphaFold. *Nature*, 596:583–589, 2021. doi: 10.1038/s41586-021-03819-2.
- [2] Minkyung Baek, Frank DiMaio, Ivan Anishchenko, Justas Dauparas, Sergey Ovchinnikov, Gyu Rie Lee, Jue Wang, Qian Cong, Lisa N. Kinch, R. Dustin Schaeffer, et al. Accurate prediction of protein structures and interactions using a three-track neural network. *Science*, 373(6557):871–876, 2021. doi: 10.1126/science.abj8754.
- [3] Brian Kuhlman and Philip Bradley. Advances in protein structure prediction and design. *Nature Reviews Molecular Cell Biology*, 20:681–697, 2019. doi: 10.1038/s41580-019-0163-x.
- [4] Po-Ssu Huang, Scott E. Boyken, and David Baker. The coming of age of de novo protein design. *Nature*, 537(7620):320–327, 2016. doi: 10.1038/nature19946.
- [5] Simon C. Potter, Aurélien Luciani, Sean R. Eddy, Youngmi Park, Rodrigo Lopez, and Robert D. Finn. HMMER web server: 2018 update. *Nucleic Acids Research*, 46(W1):W200–W204, 2018. doi: 10.1093/nar/gky448.

- [6] Anders Krogh, Michael Brown, I. Saira Mian, Kimmen Sjölander, and David Haussler. Hidden Markov models in computational biology: Applications to protein modeling. *Journal of Molecular Biology*, 235(5):1501–1531, 1994. doi: 10.1006/jmbi.1994.1104.
- [7] Faruck Morcos, Andrea Pagnani, Bryan Lunt, Arianna Bertolino, Debora S. Marks, Chris Sander, Riccardo Zecchina, José N. Onuchic, Terence Hwa, and Martin Weigt. Direct-coupling analysis of residue coevolution captures native contacts across many protein families. *Proceedings of the National Academy of Sciences*, 108(49):E1293–E1301, 2011. doi: 10.1073/pnas.1111471108.
- [8] Magnus Ekeberg, Cecilia Lövkvist, Yueheng Lan, Martin Weigt, and Erik Aurell. Improved contact prediction in proteins: Using pseudolikelihoods to infer Potts models. *Physical Review E*, 87(1):012707, 2013. doi: 10.1103/PhysRevE.87.012707.
- [9] Jeanne Trinquier, Guido Uguzzoni, Andrea Pagnani, Francesco Zamponi, and Martin Weigt. Efficient generative modeling of protein sequences using simple autoregressive models. *Nature Communications*, 12:5800, 2021. doi: 10.1038/s41467-021-25756-4.
- [10] Diederik P. Kingma and Max Welling. Auto-encoding variational Bayes. In *International Conference on Learning Representations (ICLR)*, 2014.
- [11] Adam J. Riesselman, John B. Ingraham, and Debora S. Marks. Deep generative models of genetic variation capture the effects of mutations. *Nature Methods*, 15:816–822, 2018. doi: 10.1038/s41592-018-0138-4.
- [12] Sam Sinai, Eric Kelsic, George M. Church, and Martin A. Nowak. Variational auto-encoding of protein sequences. *arXiv preprint arXiv:1712.03346*, 2017.
- [13] Noelia Ferruz, Steffen Schmidt, and Birte Höcker. ProtGPT2 is a deep unsupervised language model for protein design. *Nature Communications*, 13:4348, 2022. doi: 10.1038/s41467-022-32007-7.
- [14] Ali Madani, Ben Krause, Eric R. Greene, Subu Subramanian, Benjamin P. Mohr, James M. Holton, Jose Luis Olmos, Caïming Xiong, Zhi Zhong Sun, Richard Socher, James S. Fraser, and Nikhil Naik. Large language models generate functional protein sequences across diverse families. *Nature Biotechnology*, 41:1099–1106, 2023. doi: 10.1038/s41587-022-01618-2.
- [15] Pascal Notin, Mafalda Dias, Jonathan Frazer, Javier Marchena-Hurtado, Aidan N. Gomez, Debora Marks, and Yarin Gal. Tranception: Protein fitness prediction with autoregressive transformers and inference-time retrieval. In *Proceedings of the 39th International Conference on Machine Learning (ICML)*, pages 16990–17017, 2022.
- [16] Roshan Rao, Jason Liu, Robert Verkuil, Joshua Meier, John F. Canny, Pieter Abbeel, Tom Sercu, and Alexander Rives. MSA transformer. In *Proceedings of the 38th International Conference on Machine Learning (ICML)*, pages 8844–8856, 2021.
- [17] Sarah Alamdari, Nitya Thakkar, Rianne van den Berg, Neil Tenenholtz, Robert Strome, Alan M. Moses, Alex X. Lu, Nicolò Fusi, Ava P. Amini, and Kevin K. Yang. Protein generation with evolutionary diffusion: Sequence is all you need. *bioRxiv*, 2023. doi: 10.1101/2023.09.11.556673.
- [18] Justas Dauparas, Ivan Anishchenko, Nathaniel Bennett, Hua Bai, Robert J. Ragotte, Lukas F. Milles, Basile I.M. Wicky, Alexis Courbet, Rob J. de Haas, Neville Bethel, et al. Robust deep learning-based protein sequence design using ProteinMPNN. *Science*, 378(6615):49–56, 2022. doi: 10.1126/science.add2187.
- [19] Joseph L. Watson, David Juergens, Nathaniel R. Bennett, Brian L. Trippe, Jason Yim, Helen E. Eisenach, Woody Ahern, Andrew J. Borst, Robert J. Ragotte, Lukas F. Milles, et al. De novo design of protein structure and function with RFDiffusion. *Nature*, 620(7976):1089–1100, 2023. doi: 10.1038/s41586-023-06415-8.
- [20] Jaina Mistry, Sara Chuguransky, Lowri Williams, Matloob Qureshi, Gustavo A Salazar, Erik L L Sonnhammer, Silvio C E Tosatto, Lisanna Paladin, Shriya Raj, Lorna J Richardson, Robert D Finn, and Alex Bateman. Pfam: The protein families database in 2021. *Nucleic Acids Research*, 49(D1):D412–D419, 2021. doi: 10.1093/nar/gkaa913.

- [21] Kevin K. Yang, Zachary Wu, and Frances H. Arnold. Machine-learning-guided directed evolution for protein engineering. *Nature Methods*, 16:687–694, 2019. doi: 10.1038/s41592-019-0496-6.
- [22] Ashish Vaswani, Noam Shazeer, Niki Parmar, Jakob Uszkoreit, Llion Jones, Aidan N. Gomez, Łukasz Kaiser, and Illia Polosukhin. Attention is all you need. In *Advances in Neural Information Processing Systems*, volume 30, pages 5998–6008, 2017.
- [23] Hubert Ramsauer, Bernhard Schäfl, Johannes Lehner, Philipp Seidl, Michael Widrich, Thomas Adler, Lukas Gruber, Markus Holzleitner, Milena Pavlović, Geir Kjetil Sandve, Victor Greiff, David Kreil, Michael Kopp, Günter Klambauer, Johannes Brandstetter, and Sepp Hochreiter. Hopfield networks is all you need. In *International Conference on Learning Representations (ICLR)*, 2021.
- [24] Dmitry Krotov and John J. Hopfield. Dense associative memory for pattern recognition. In *Advances in Neural Information Processing Systems*, volume 29, 2016.
- [25] John J. Hopfield. Neural networks and physical systems with emergent collective computational abilities. *Proceedings of the National Academy of Sciences*, 79(8):2554–2558, 1982. doi: 10.1073/pnas.79.8.2554.
- [26] Daniel J. Amit, Hanoch Gutfreund, and Haim Sompolinsky. Storing infinite numbers of patterns in a spin-glass model of neural networks. *Physical Review Letters*, 55(14):1530–1533, 1985. doi: 10.1103/PhysRevLett.55.1530.
- [27] Yang Song and Stefano Ermon. Generative modeling by estimating gradients of the data distribution. In *Advances in Neural Information Processing Systems*, volume 32, 2019.
- [28] Yang Song, Jascha Sohl-Dickstein, Diederik P. Kingma, Abhishek Kumar, Stefano Ermon, and Ben Poole. Score-based generative modeling through stochastic differential equations. In *International Conference on Learning Representations (ICLR)*, 2021.
- [29] Jonathan Ho, Ajay Jain, and Pieter Abbeel. Denoising diffusion probabilistic models. In *Advances in Neural Information Processing Systems*, volume 33, pages 6840–6851, 2020.
- [30] Max Welling and Yee Whye Teh. Bayesian learning via stochastic gradient Langevin dynamics. In *Proceedings of the 28th International Conference on Machine Learning (ICML)*, pages 681–688, 2011.
- [31] Benjamin Hoover, Yuchen Liang, Bao Pham, Rameswar Panda, Hendrik Strobelt, Duen Horng Chau, Mohammed J. Zaki, and Dmitry Krotov. Energy transformer. In *Advances in Neural Information Processing Systems*, volume 36, 2023.
- [32] Alain Durmus and Éric Moulines. Nonasymptotic convergence analysis for the unadjusted Langevin algorithm. *The Annals of Applied Probability*, 27(3):1551–1587, 2017. doi: 10.1214/16-AAP1238.
- [33] Arnak S. Dalalyan. Theoretical guarantees for approximate sampling from smooth and log-concave densities. *Journal of the Royal Statistical Society: Series B*, 79(3):651–676, 2017. doi: 10.1111/rssb.12183.
- [34] Abdulrahman Alswaidan and Jeffrey D. Varner. Stochastic attention via Langevin dynamics on the modern Hopfield energy. *arXiv preprint arXiv:2603.06875*, 2026. doi: 10.48550/arXiv.2603.06875.
- [35] Zeming Lin, Halil Akin, Roshan Rao, Brian Hie, Zhongkai Zhu, Wenting Lu, Nikita Smetanin, Robert Verkuil, Ori Kabeli, Yaniv Shmueli, Allan Costa, Maryam Fazel-Zarandi, Tom Sercu, Sal Candido, and Alexander Rives. Evolutionary-scale prediction of atomic-level protein structure with a language model. *Science*, 379(6637):1123–1130, 2023. doi: 10.1126/science.ade2574.
- [36] Yang Zhang and Jeffrey Skolnick. TM-align: a protein structure alignment algorithm based on the TM-score. *Nucleic Acids Research*, 33(7):2302–2309, 2005. doi: 10.1093/nar/gki524.

- [37] Richard N. McLaughlin, Frank J. Poelwijk, Arjun Raman, Walraj S. Gosal, and Rama Ranganathan. The spatial architecture of protein function and adaptation. *Nature*, 491:138–142, 2012. doi: 10.1038/nature11500.
- [38] André J. Faure, Javier Domingo, Joern M. Schmiedel, Cristina Hidalgo-Carcedo, Guillaume Diss, and Ben Lehner. Mapping the energetic and allosteric landscapes of protein binding domains. *Nature*, 604:175–183, 2022. doi: 10.1038/s41586-022-04586-4.
- [39] Brian P. Lazzaro, Michael Zasloff, and Jens Rolff. Antimicrobial peptides: Application informed by evolution. *Science*, 368(6490):eaau5480, 2020. doi: 10.1126/science.aau5480.
- [40] David H. Ackley, Geoffrey E. Hinton, and Terrence J. Sejnowski. A learning algorithm for Boltzmann machines. *Cognitive Science*, 9(1):147–169, 1985. doi: 10.1207/s15516709cog0901\_7.
- [41] Gareth O. Roberts and Richard L. Tweedie. Exponential convergence of Langevin distributions and their discrete approximations. *Bernoulli*, 2(4):341–363, 1996. doi: 10.2307/3318418.
- [42] Anton Bovier, Michael Eckhoff, Véronique Gayrard, and Markus Klein. Metastability in reversible diffusion processes I: Sharp asymptotics for capacities and exit times. *Journal of the European Mathematical Society*, 6(4):399–424, 2004. doi: 10.4171/JEMS/14.
- [43] Milot Mirdita, Konstantin Schütze, Yoshitaka Moriwaki, Lim Heo, Sergey Ovchinnikov, and Martin Steinegger. ColabFold: Making protein folding accessible to all. *Nature Methods*, 19: 679–682, 2022. doi: 10.1038/s41592-022-01488-1.

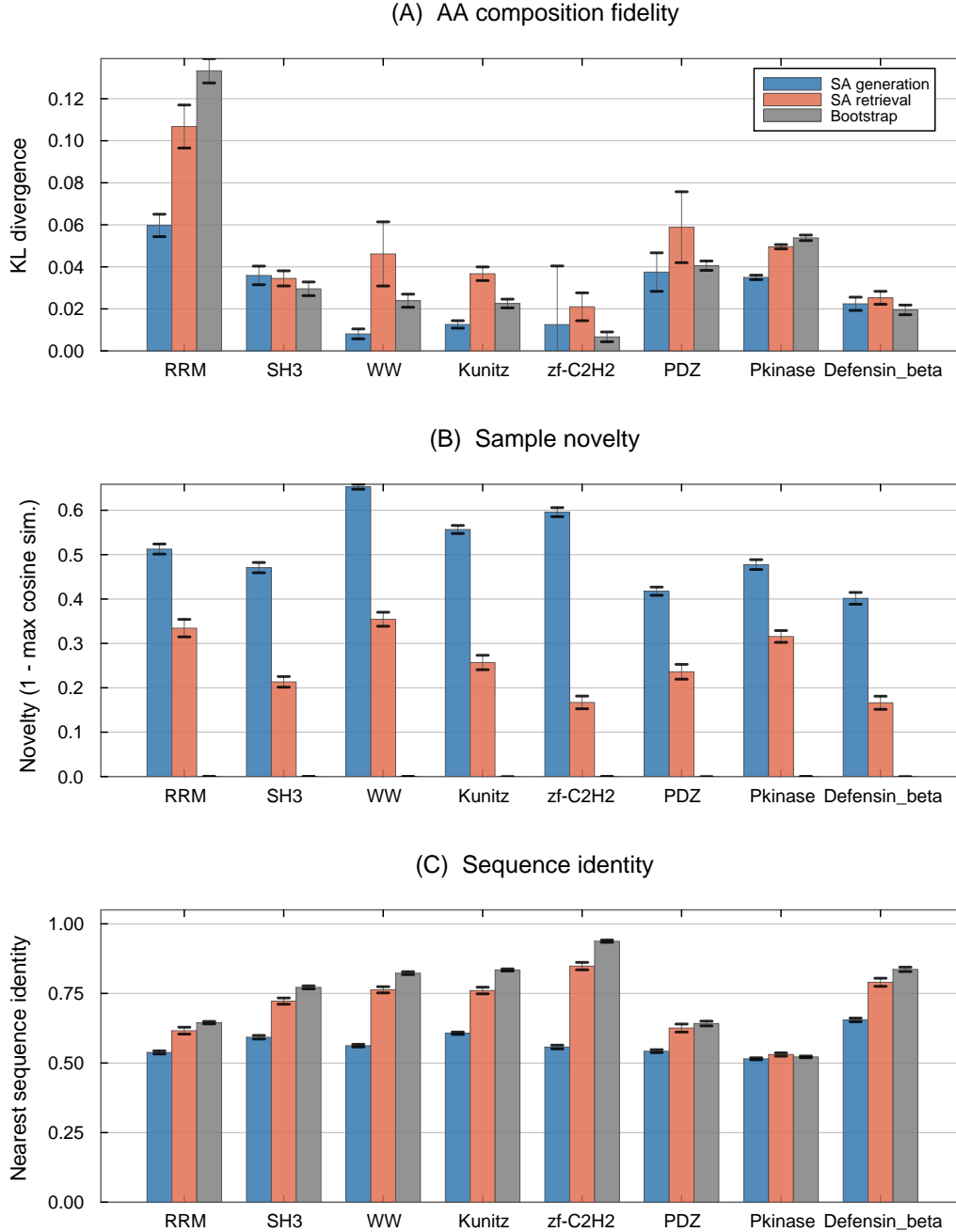


Figure 1: Cross-family comparison of SA generation, SA retrieval, and bootstrap across eight Pfam families. **(A)** KL divergence of amino acid composition (lower is better). SA generation achieves the lowest or near-lowest KL in every family. **(B)** Novelty in PCA space ( $1 - \max_k \cos(\hat{\xi}, \mathbf{m}_k)$ ); higher is better). SA generation produces substantially novel sequences, while bootstrap samples, which are exact copies of stored patterns, have zero PCA-space novelty by construction. **(C)** Nearest sequence identity to a stored pattern (lower indicates greater departure). Error bars show  $\pm 1$  SE (30 chains  $\times$  5 samples).

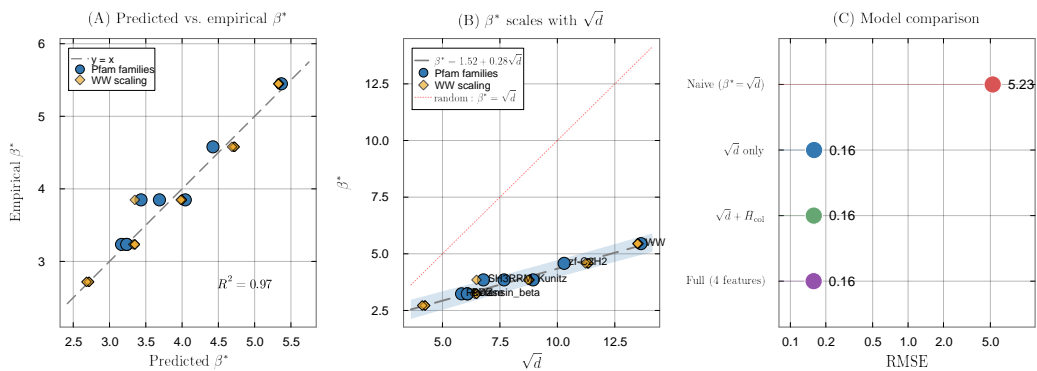


Figure 2: Predicting the critical temperature from MSA statistics. **(A)** Predicted vs. empirical  $\beta^*$  for the simple linear model  $\beta^* \approx 1.57 + 0.28\sqrt{d}$  ( $R^2=0.97$ ,  $n=33$ ). Blue circles: eight Pfam families; gold diamonds: WW scaling replicates ( $K \in \{20, \dots, 400\}$ , five repeats each). **(B)**  $\beta^*$  as a function of  $\sqrt{d}$ , with the fitted regression (dashed) and the random-pattern prediction  $\beta^* = \sqrt{d}$  (dotted red). The intercept offset and reduced slope reflect structured correlations in real protein families. **(C)** Model comparison (log-scale RMSE). The simple  $\sqrt{d}$  model (RMSE=0.16) is  $33\times$  more accurate than the naive random-pattern prediction  $\beta^* = \sqrt{d}$  (RMSE=5.29); adding MSA features provides negligible improvement.

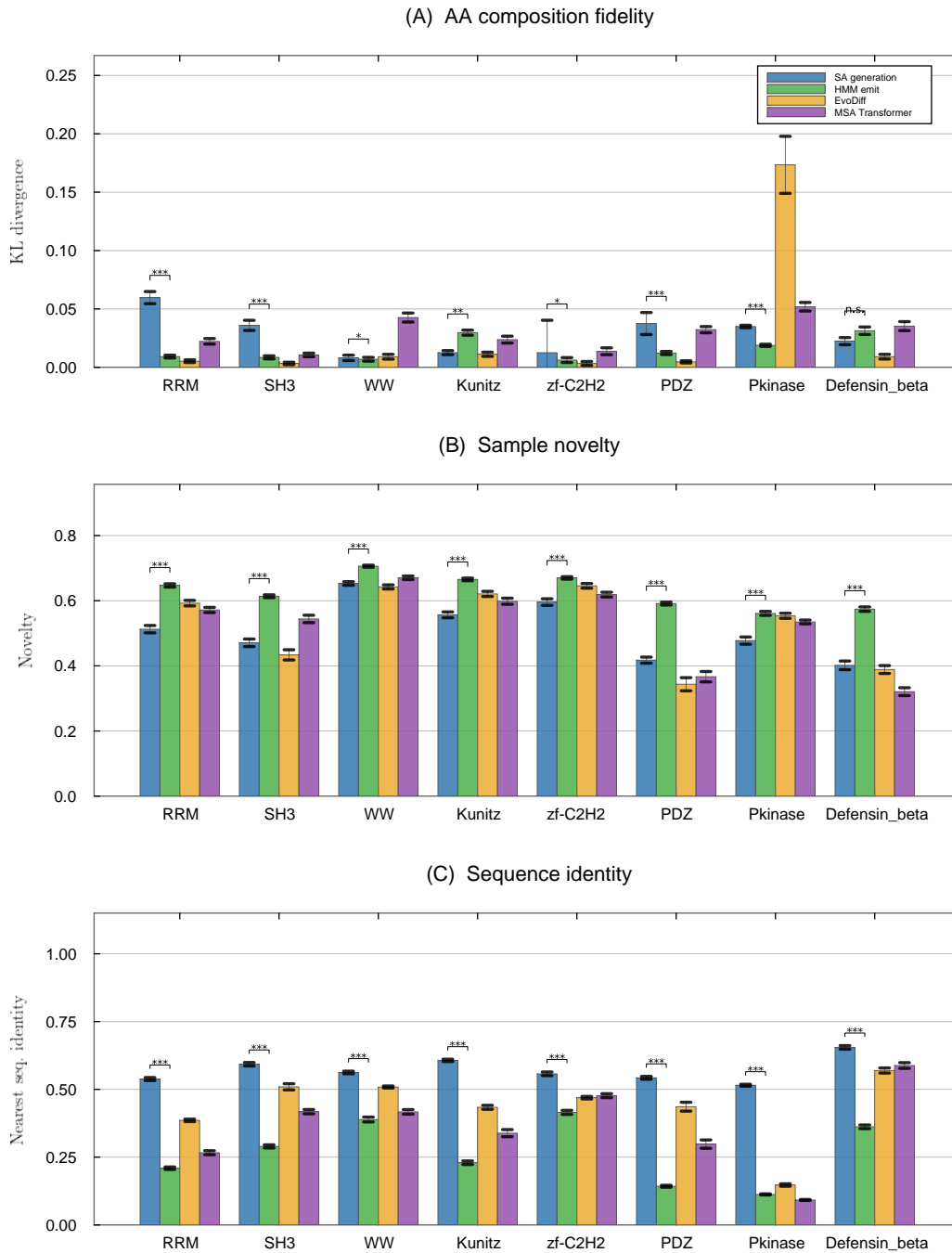


Figure 3: Head-to-head comparison of SA generation against three learned baselines (profile HMM emit, EvoDiff, MSA Transformer) across all eight Pfam families. **(A)** KL divergence of amino acid composition (pooled over all 150 generated sequences, with bootstrap SE;  $n_{boot}=1000$ ). **(B)** Novelty in PCA space. **(C)** Nearest sequence identity. Panels (B) and (C) report per-chain means  $\pm 1$  SE (30 chains  $\times$  5 samples). Simple reference baselines (Gaussian perturbation, convex combination, stored-pattern retrieval) are omitted from this figure because their design precludes meaningful comparison: retrieval returns memorized sequences (novelty  $\approx 0$ , identity  $\approx 1$ ) and the perturbation baselines do not attempt to model the family distribution. Their metrics are reported in SI Appendix, Table S2 for completeness.

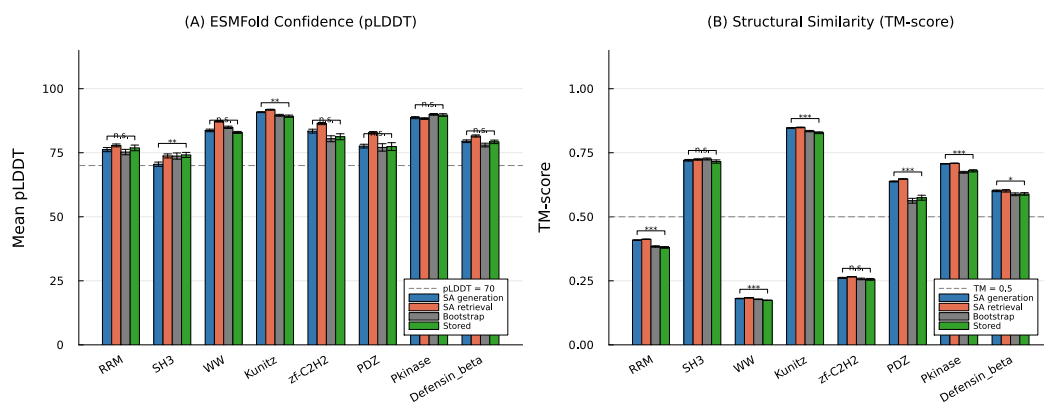


Figure 4: Structure validation of SA-generated sequences using ESMFold. **(A)** Mean pLDDT (folding confidence) across all eight Pfam families for SA generation, SA retrieval, bootstrap, and stored (natural) sequences. The dashed line indicates the pLDDT=70 confidence threshold. **(B)** TM-score to a representative experimentally determined structure for each family. The dashed line indicates TM=0.5 (same-fold threshold). Significance brackets show Wilcoxon rank-sum tests comparing SA generation to stored sequences: \*\*\* $p < 0.001$ , \*\* $p < 0.01$ , \* $p < 0.05$ , n.s. = not significant. Error bars show  $\pm 1$  SE ( $n=50$  sequences per condition).

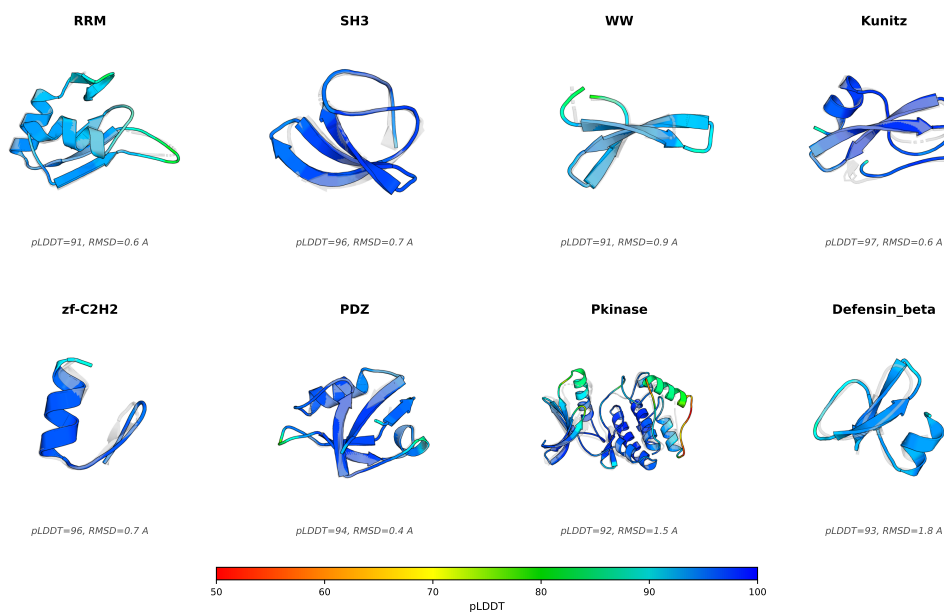


Figure 5: AlphaFold2 predicted structures for representative SA-generated sequences (colored by per-residue pLDDT confidence) superimposed on the experimentally determined reference structure for each family (gray, semi-transparent). For each family, the SA-generated sequence with the highest mean pLDDT was selected and aligned to the reference using PyMOL. The close predicted structural agreement (sub-angstrom RMSD) and uniformly high pLDDT scores are consistent with SA-generated sequences, despite substantial sequence-level novelty, encoding three-dimensional folds that recapitulate the canonical architecture of their target family, though experimental structure determination would be needed for definitive confirmation.

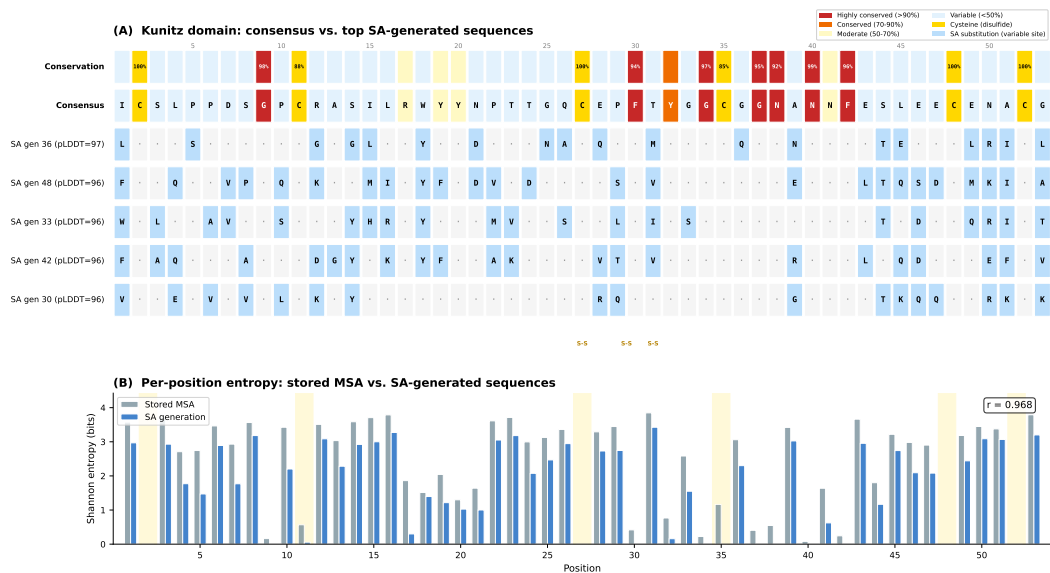


Figure 6: Sequence-level analysis of SA-generated Kunitz domain sequences. **(A)** Alignment of the family consensus with the five highest-confidence SA-generated sequences (ranked by AlphaFold2 pLDDT). Positions are colored by conservation in the stored MSA: highly conserved ( $> 90\%$ , red), conserved (70–90%, orange), moderate (50–70%, yellow), and variable ( $< 50\%$ , blue). Cysteines forming the three disulfide bonds are highlighted in gold. Dots indicate matches to the consensus; letters indicate substitutions. All five sequences preserve every highly conserved position (11/11) and all six cysteines (6/6), while introducing 17–25 substitutions concentrated at variable sites. **(B)** Per-position Shannon entropy for the stored MSA (gray) and SA-generated sequences (blue). The strong correlation ( $r=0.968$ ) indicates that SA recapitulates the position-specific conservation pattern of the family: structurally critical positions remain invariant, while evolutionarily permissive positions exhibit comparable diversity.

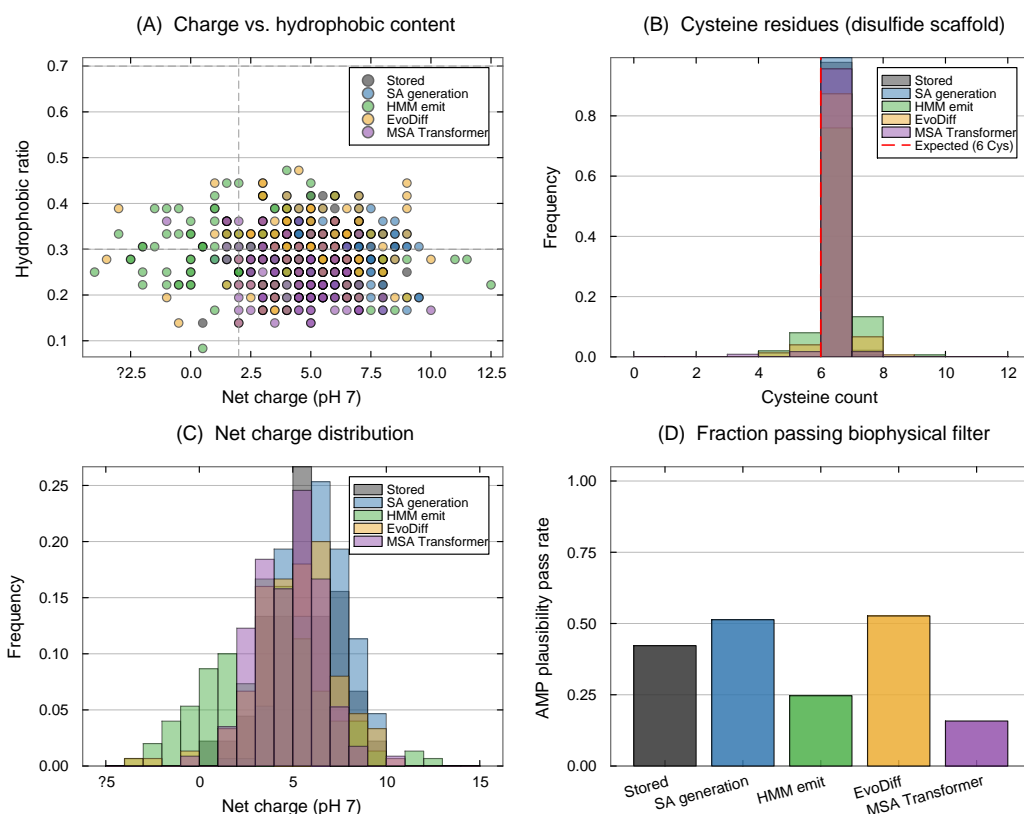


Figure 7: Biophysical properties of beta defensin sequences (PF00711). **(A)** Net charge at pH 7 vs. hydrophobic residue fraction. SA-generated sequences (blue) overlap the stored natural sequences (gray), while HMM emit (green) and MSA Transformer (purple) drift to lower charge. Dashed lines indicate the antimicrobial plausibility thresholds (charge  $\geq +2$ , hydrophobic fraction 0.3–0.7). **(B)** Cysteine count distribution. SA generation preserves the six-cysteine disulfide scaffold (red dashed line) with the same fidelity as the stored alignment. **(C)** Net charge distribution. SA generation produces a charge profile closely matching stored sequences. **(D)** Fraction of sequences passing a minimal biophysical plausibility filter (charge  $\geq +2$ , hydrophobic fraction  $\in [0.3, 0.7]$ ,  $\geq 4$  cysteines).

Table 1: Properties of the eight Pfam families used in this study.  $K$ : number of seed sequences after cleaning.  $L$ : alignment length (columns retained).  $d$ : PCA dimension (95% variance).  $\bar{H}_{\text{col}}$ : mean per-column Shannon entropy (nats).  $K_{\text{eff}}$ : effective number of sequences at 80% identity threshold.  $\beta^*$ : empirical entropy inflection point.  $\beta^*/\sqrt{d}$ : ratio to the random-pattern prediction.

Family	Pfam ID	$K$	$L$	$d$	$\bar{H}_{\text{col}}$	$K_{\text{eff}}$	$\beta^*$	$\beta^*/\sqrt{d}$
RRM	PF00076	68	71	59	1.92	68	3.85	0.50
SH3	PF00018	55	48	46	1.68	55	3.85	0.57
WW	PF00397	420	31	186	1.74	419	5.45	0.40
Kunitz	PF00014	99	53	80	1.61	99	3.85	0.43
zf-C2H2	PF00096	151	23	106	1.91	151	4.58	0.44
PDZ	PF00595	44	83	37	1.88	43	3.23	0.53
Pkinase	PF00069	37	262	34	1.72	37	3.23	0.55
Defensin_beta	PF00711	45	36	37	1.65	45	3.23	0.53

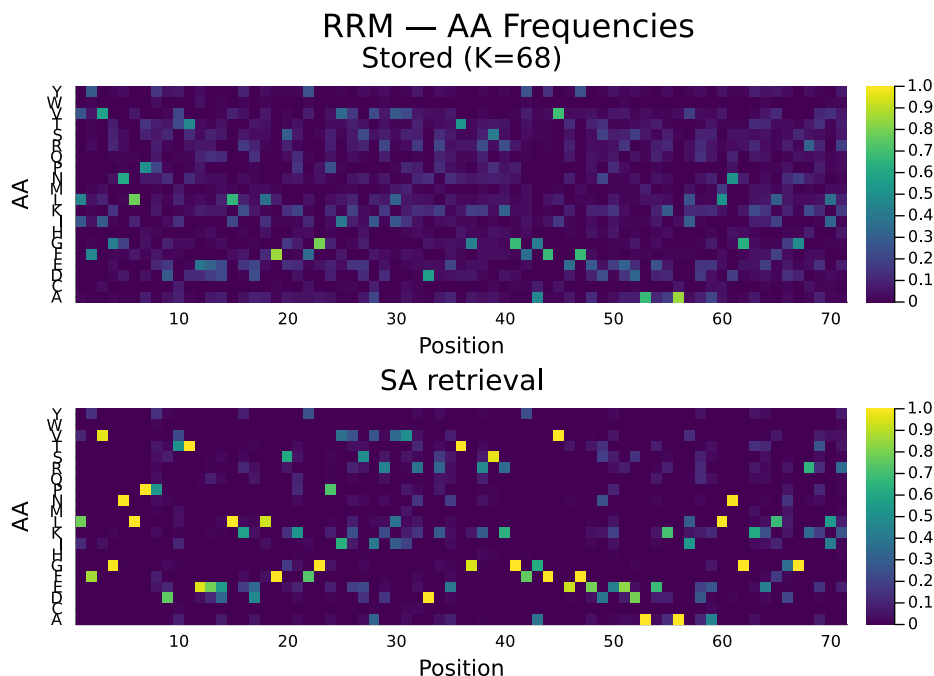


Figure S1: Per-position amino acid frequency profiles for the RRM family (PF00076). **Top:** stored seed sequences ( $K=68$ ). **Bottom:** SA-generated sequences ( $S=150$ , retrieval regime). The generated ensemble reproduces the position-specific conservation pattern of the family, including strongly conserved positions and variable regions.

## SI Appendix

### S1 Amino Acid Composition Profiles

We compared the per-position amino acid frequency profiles of the stored seed sequences and SA-generated sequences for the RRM family (PF00076, Fig. S1). We found that the generated ensemble faithfully reproduces the conservation pattern of the family: strongly conserved positions (e.g., the aromatic residues characteristic of the ribonucleoprotein motifs RNP1 and RNP2) retain high frequency in the generated output, while variable positions display a similar breadth of amino acid usage. This agreement is consistent with the low KL divergences reported in Table S2 and shows that the Boltzmann sampling procedure captures not only global amino acid composition but also the position-specific constraints encoded in the seed alignment.

### S2 Scaling Study

To characterize how generation quality degrades with decreasing family size, we subsampled the WW domain ( $K=420$ ) at  $K \in \{20, 50, 100, 200, 400\}$  with five independent replicates per condition (Fig. S2). Stochastic attention in the generation regime maintained low KL divergence across the entire range ( $0.019 \pm 0.008$  at  $K=20$ , improving to  $0.010 \pm 0.002$  at  $K=400$ ), while the convex combination baseline exceeded  $\text{KL}=0.8$  at every family size. Novelty increased with  $K$  (from 0.47 to 0.74), reflecting the richer landscape of a larger memory set, while nearest sequence identity decreased correspondingly (from 0.71 to 0.56). The empirical critical temperature  $\beta^*$  increased from 2.7 at  $K=20$  to 5.5 at  $K=400$ , tracking the growth in PCA dimensionality.

### S3 Multi-Family Scaling at $K=20$

The WW-only scaling study (Section S2) demonstrated that SA generation quality is robust down to  $K=20$ , but a single family cannot establish generality. To test whether this robustness holds

across families with different sequence lengths, conservation levels, and PCA dimensionalities, we subsampled three additional families to  $K=20$  with five independent replicates each: SH3 ( $K_{\text{full}}=55$ ,  $L=48$ ), Kunitz ( $K_{\text{full}}=99$ ,  $L=53$ ), and zf-C2H2 ( $K_{\text{full}}=151$ ,  $L=23$ ). All SA parameters were identical to the main experiment; PCA and  $\beta^*$  were recomputed from scratch for each subsample.

Table S1 reports the results alongside the original WW subsamples at  $K=20$ . Stochastic attention maintained low KL divergence (0.013–0.026), substantial novelty (0.46–0.47), and moderate sequence identity (0.67–0.73) across all four families at  $K=20$ , with narrow standard deviations across the five replicates. The consistency of these metrics across families that differ in length by an order of magnitude (zf-C2H2:  $L=23$  vs. WW:  $L=31$  vs. Kunitz:  $L=53$ ) confirms that the entropy inflection criterion successfully adapts the operating temperature to each family’s geometry, and that the robustness observed in the WW scaling study is not family-specific.

Table S1: SA generation quality at  $K=20$  across four Pfam families (five independent subsamples each). Values are mean  $\pm$  SD over the five replicates.

Family	$K_{\text{full}}$	$L$	$d_{\text{PCA}}$	KL	Novelty	Seq. ID
SH3	55	48	17–18	$0.026 \pm 0.003$	$0.46 \pm 0.01$	$0.67 \pm 0.01$
Kunitz	99	53	17–18	$0.020 \pm 0.004$	$0.47 \pm 0.01$	$0.72 \pm 0.01$
zf-C2H2	151	23	18	$0.013 \pm 0.004$	$0.47 \pm 0.01$	$0.73 \pm 0.00$
WW	420	31	17–18	$0.019 \pm 0.008$	$0.47 \pm 0.01$	$0.71 \pm 0.02$

## S4 Generation Metrics

Table S2 reports the full generation metrics for all eight Pfam families across five sampling conditions: SA generation ( $\beta \approx 2\beta^*$ ), SA retrieval ( $\beta \approx 20\beta^*$ ), bootstrap resampling, Gaussian perturbation, and convex combination. For each condition, we report the KL divergence of amino acid composition, PCA-space cosine novelty, and nearest sequence identity to a stored pattern. Standard errors are computed over 30 independent Langevin chains of 5 samples each; KL standard errors are obtained via 1,000-fold bootstrap resampling. Bold entries indicate the best-performing method for each family and metric.

## S5 AlphaFold2 Cross-Validation of Structure Predictions

Figure S3 shows pLDDT and TM-score results from both ESMFold and AlphaFold2 side by side across all eight families. The two predictors produce qualitatively identical patterns: SA-generated sequences achieve pLDDT well above the 70 threshold in every family under both predictors, and the family-to-family ordering of TM-scores is preserved. Figure S4 quantifies the agreement directly. TM-scores are in near-perfect agreement across predictors (Pearson  $r=0.999$ ), confirming that the structural ranking of conditions is not an artifact of ESMFold’s architecture or training data. The pLDDT concordance is more moderate ( $r=0.434$ ), reflecting the fact that each predictor has its own confidence calibration scale; AlphaFold2 pLDDT values are systematically higher than ESMFold values for the same sequences (points lie above the identity line in Fig. S4A), consistent with known differences in the two models’ confidence scoring. The near-perfect TM-score concordance is the key finding: it confirms that the structural conclusions drawn from ESMFold in the main text are not predictor-specific.

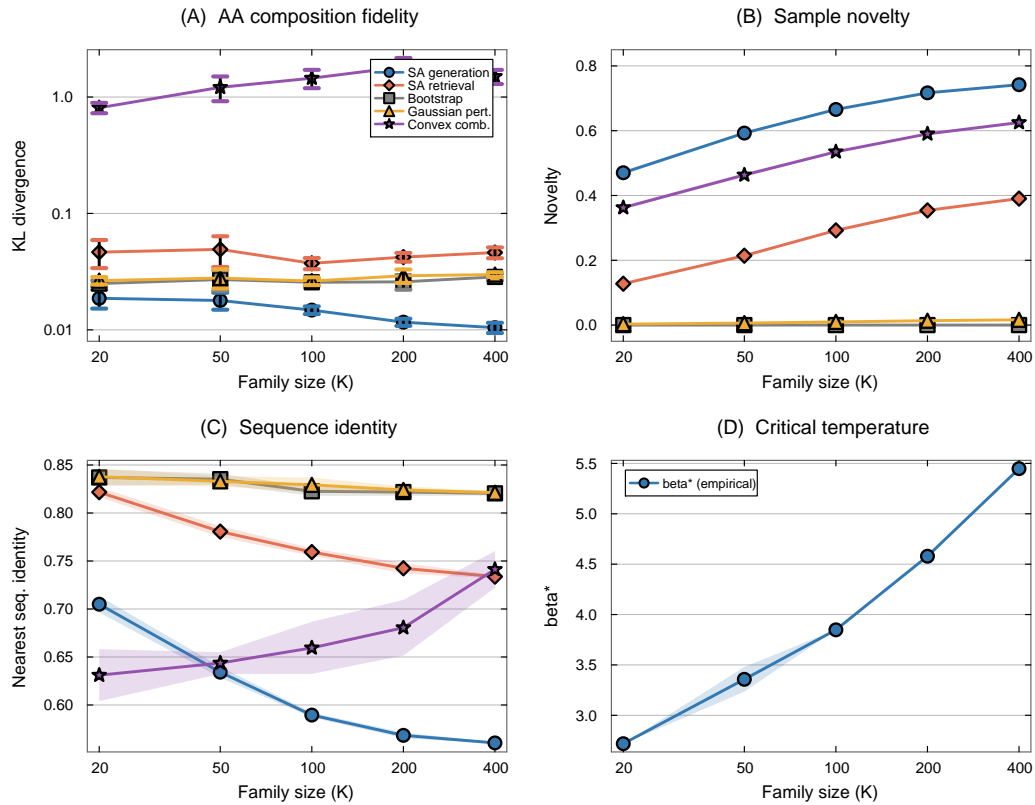


Figure S2: Scaling study: WW domain subsampled at  $K \in \{20, 50, 100, 200, 400\}$  with five independent replicates. **(A)** KL divergence (log–log scale). SA generation maintains low KL across the entire range; convex combination degrades catastrophically. **(B)** Novelty increases with  $K$  for SA methods; baselines remain near zero. **(C)** Nearest sequence identity decreases with  $K$ , indicating the sampler explores further from stored patterns as more patterns shape the energy landscape. **(D)** The empirical critical temperature  $\beta^*$  increases with family size. Shaded regions and error bars show  $\pm 1$  SE.

Table S2: Generation metrics across eight Pfam families (mean  $\pm$  SE). SA gen: stochastic attention generation regime ( $\beta \approx 2\beta^*$ ). SA ret: retrieval regime ( $\beta \approx 20\beta^*$ ). BS: bootstrap. GP: Gaussian perturbation. CC: convex combination. KL: KL divergence of amino acid composition ( $\downarrow$  lower is better; SE via 1,000-fold bootstrap). Novelty:  $1 - \max_k \cos(\hat{\xi}, \mathbf{m}_k)$  in PCA space ( $\uparrow$  higher is better). SeqID: nearest sequence identity to a stored pattern after decoding ( $\downarrow$  lower is better, indicating greater novelty). Standard errors for novelty and SeqID are computed over 30 independent chains of 5 samples each.

Family	Method	KL <sub>AA</sub> ( $\downarrow$ )	Novelty ( $\uparrow$ )	SeqID ( $\downarrow$ )
RRM	SA gen	<b>0.060 <math>\pm</math> 0.005</b>	<b>0.513 <math>\pm</math> 0.011</b>	<b>0.538 <math>\pm</math> 0.006</b>
	SA ret	0.107 $\pm$ 0.010	0.334 $\pm$ 0.020	0.616 $\pm$ 0.012
	BS	0.133 $\pm$ 0.006	0.000 $\pm$ 0.000	0.645 $\pm$ 0.004
	GP	0.132 $\pm$ 0.005	0.008 $\pm$ 0.000	0.633 $\pm$ 0.006
	CC	2.091 $\pm$ 0.000	0.510 $\pm$ 0.009	0.562 $\pm$ 0.000
SH3	SA gen	0.036 $\pm$ 0.004	<b>0.471 <math>\pm</math> 0.012</b>	<b>0.593 <math>\pm</math> 0.006</b>
	SA ret	0.035 $\pm$ 0.004	0.213 $\pm$ 0.012	0.722 $\pm$ 0.011
	BS	<b>0.030 <math>\pm</math> 0.003</b>	0.000 $\pm$ 0.000	0.772 $\pm$ 0.006
	GP	<b>0.030 <math>\pm</math> 0.003</b>	0.006 $\pm$ 0.000	0.752 $\pm$ 0.006
	CC	0.798 $\pm$ 0.012	0.474 $\pm$ 0.008	0.601 $\pm$ 0.002
WW	SA gen	<b>0.008 <math>\pm</math> 0.002</b>	<b>0.653 <math>\pm</math> 0.006</b>	<b>0.562 <math>\pm</math> 0.005</b>
	SA ret	0.046 $\pm$ 0.013	0.354 $\pm$ 0.016	0.763 $\pm$ 0.011
	BS	0.024 $\pm$ 0.003	0.000 $\pm$ 0.000	0.823 $\pm$ 0.005
	GP	0.029 $\pm$ 0.004	0.017 $\pm$ 0.000	0.809 $\pm$ 0.006
	CC	1.375 $\pm$ 0.092	0.637 $\pm$ 0.004	0.766 $\pm$ 0.001
Kunitz	SA gen	<b>0.013 <math>\pm</math> 0.002</b>	<b>0.557 <math>\pm</math> 0.009</b>	<b>0.607 <math>\pm</math> 0.004</b>
	SA ret	0.037 $\pm$ 0.003	0.257 $\pm$ 0.016	0.760 $\pm$ 0.012
	BS	0.023 $\pm$ 0.002	0.000 $\pm$ 0.000	0.834 $\pm$ 0.004
	GP	0.024 $\pm$ 0.002	0.010 $\pm$ 0.000	0.844 $\pm$ 0.004
	CC	0.721 $\pm$ 0.013	0.546 $\pm$ 0.007	0.590 $\pm$ 0.001
zf-C2H2	SA gen	0.013 $\pm$ 0.028	<b>0.596 <math>\pm</math> 0.010</b>	<b>0.557 <math>\pm</math> 0.007</b>
	SA ret	0.021 $\pm$ 0.010	0.167 $\pm$ 0.014	0.848 $\pm$ 0.013
	BS	<b>0.007 <math>\pm</math> 0.002</b>	0.000 $\pm$ 0.000	0.938 $\pm$ 0.004
	GP	<b>0.007 <math>\pm</math> 0.002</b>	0.011 $\pm$ 0.000	0.940 $\pm$ 0.004
	CC	2.346 $\pm$ 0.060	0.580 $\pm$ 0.006	0.600 $\pm$ 0.001
PDZ	SA gen	<b>0.038 <math>\pm</math> 0.010</b>	<b>0.418 <math>\pm</math> 0.009</b>	<b>0.543 <math>\pm</math> 0.005</b>
	SA ret	0.059 $\pm$ 0.016	0.236 $\pm$ 0.017	0.626 $\pm$ 0.014
	BS	0.041 $\pm$ 0.002	0.000 $\pm$ 0.000	0.642 $\pm$ 0.009
	GP	0.045 $\pm$ 0.003	0.006 $\pm$ 0.000	0.648 $\pm$ 0.007
	CC	0.339 $\pm$ 0.001	0.449 $\pm$ 0.009	0.549 $\pm$ 0.001
Pkinase	SA gen	<b>0.035 <math>\pm</math> 0.001</b>	<b>0.478 <math>\pm</math> 0.011</b>	0.515 $\pm$ 0.004
	SA ret	0.050 $\pm$ 0.001	0.316 $\pm$ 0.013	0.531 $\pm$ 0.006
	BS	0.054 $\pm$ 0.001	0.000 $\pm$ 0.000	0.522 $\pm$ 0.003
	GP	0.051 $\pm$ 0.001	0.005 $\pm$ 0.000	0.533 $\pm$ 0.003
	CC	0.062 $\pm$ 0.001	0.446 $\pm$ 0.009	<b>0.470 <math>\pm</math> 0.000</b>
Defensin_beta	SA gen	<b>0.022 <math>\pm</math> 0.004</b>	<b>0.402 <math>\pm</math> 0.013</b>	<b>0.655 <math>\pm</math> 0.007</b>
	SA ret	0.025 $\pm$ 0.008	0.166 $\pm$ 0.015	0.790 $\pm$ 0.015
	BS	0.020 $\pm$ 0.003	0.000 $\pm$ 0.000	0.836 $\pm$ 0.006
	GP	0.023 $\pm$ 0.003	0.006 $\pm$ 0.000	0.835 $\pm$ 0.006
	CC	0.708 $\pm$ 0.001	0.442 $\pm$ 0.009	0.716 $\pm$ 0.001

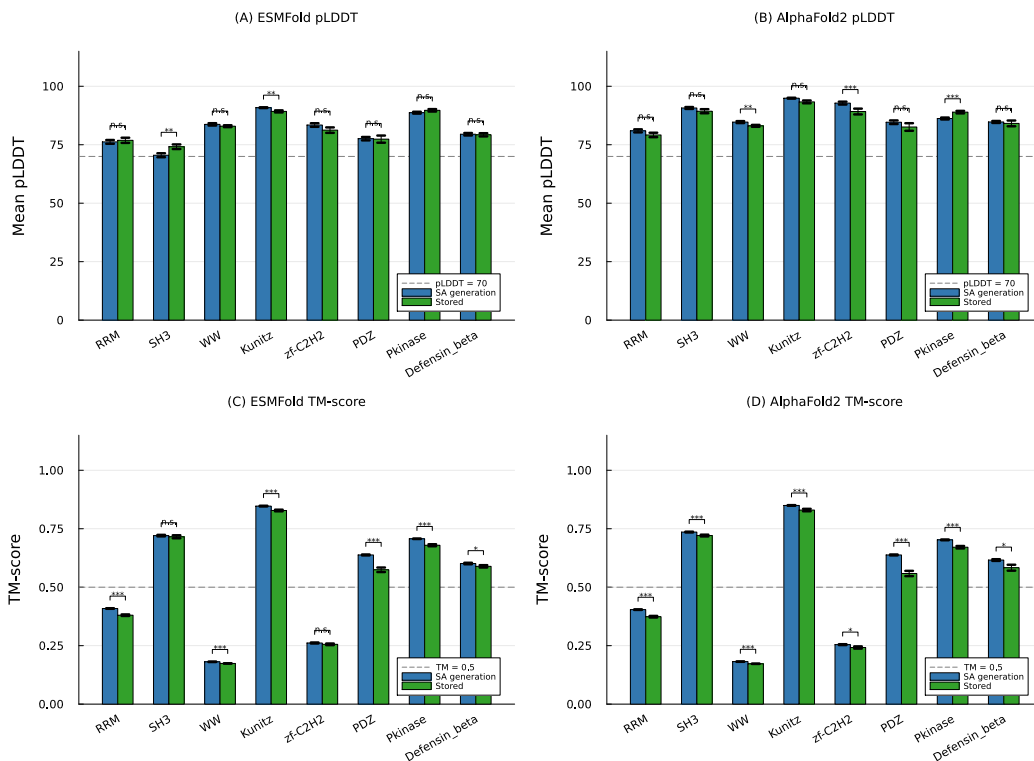


Figure S3: Structure validation results from ESMFold (A, C) and AlphaFold2 (B, D) across all eight Pfam families. (A, B) Mean pLDDT for SA-generated (blue) and stored (green) sequences; dashed line at pLDDT=70. (C, D) Mean TM-score to the family reference structure; dashed line at TM=0.5. Significance brackets show Wilcoxon rank-sum tests comparing SA generation to stored sequences. The two predictors produce qualitatively identical patterns across all families, confirming that the structural conclusions are not predictor-specific.

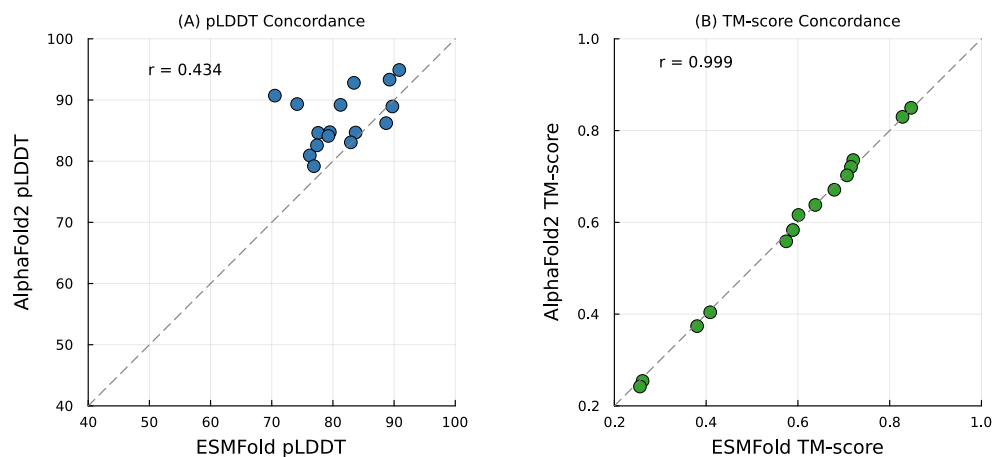


Figure S4: Concordance between ESMFold and AlphaFold2 structure predictions for SA-generated sequences across all eight families. Each point is one family-condition pair. (A) pLDDT concordance ( $r=0.434$ ); AlphaFold2 pLDDT values are systematically higher, reflecting differences in confidence calibration between the two models. (B) TM-score concordance ( $r=0.999$ ); points lie on the identity line, confirming that the two predictors rank conditions identically and that the TM-score conclusions are robust to the choice of structure predictor.

## S6 Independent Fitness Validation via ESM2

As an independent assessment of whether SA-generated sequences resemble natural proteins, we scored all generated and stored sequences using ESM2-650M [35], a protein language model pre-trained on millions of UniRef50 sequences that is entirely independent of the stochastic attention framework. For each sequence, we computed the pseudo-perplexity via masked marginal scoring: each position was masked in turn, the model predicted a distribution over amino acids, and the log-probability of the true residue was recorded. The pseudo-perplexity (lower is more protein-like) is  $\exp(-\frac{1}{L} \sum_{\ell=1}^L \log P(a_{\ell} | \mathbf{a}_{\setminus \ell}))$ , where  $a_{\ell}$  is the amino acid at position  $\ell$  and  $\mathbf{a}_{\setminus \ell}$  denotes all other positions. Wilcoxon rank-sum tests with Cohen’s  $d$  effect sizes compared SA-generated sequences ( $n=150$ ) to stored natural sequences ( $n=37-50$ ) for each family (Table S3).

SA-generated sequences were statistically indistinguishable from natural family members in four of eight families (Wilcoxon  $p > 0.05$ ; RRM, zf-C2H2, Pkinase, Defensin\_beta:  $p > 0.29$ ). In the Kunitz domain, SA generation achieved significantly *lower* (better) pseudo-perplexity than stored sequences (4.47 vs. 4.98,  $p < 0.001$ ,  $d=-0.74$ ). Three families showed modestly higher pseudo-perplexity for SA generation (SH3:  $d=0.60$ ; WW:  $d=1.03$ ; PDZ:  $d=0.60$ ), though all SA-generated sequences remained well within the range of natural protein sequences. The overall mean pseudo-perplexity across all families was 5.71 for SA-generated sequences versus 5.58 for stored sequences, confirming that an independent protein language model trained on billions of sequences considers SA-generated sequences to be comparably protein-like to natural family members.

Table S3: ESM2-650M pseudo-perplexity validation. Lower pseudo-perplexity indicates a more protein-like sequence.  $p$ : Wilcoxon rank-sum test (two-sided).  $d$ : Cohen’s effect size (negative values indicate SA is better). Significance: \*\*\* $p < 0.001$ , \*\* $p < 0.01$ , n.s. = not significant ( $p > 0.05$ ).

Family	SA gen ppl	Stored ppl	$p$	$d$	Sig.
RRM	4.87 ± 0.68	5.20 ± 1.92	0.30	-0.29	n.s.
SH3	5.24 ± 0.82	4.62 ± 1.48	< 0.001	0.60	***
WW	6.78 ± 1.77	5.04 ± 1.36	< 0.001	1.03	***
Kunitz	4.47 ± 0.57	4.98 ± 0.94	< 0.001	-0.74	***
zf-C2H2	7.26 ± 1.66	8.10 ± 3.47	0.41	-0.37	n.s.
PDZ	6.30 ± 1.21	5.31 ± 2.61	0.002	0.60	**
Pkinase	4.44 ± 0.32	4.32 ± 0.80	0.39	0.27	n.s.
Defensin_beta	6.35 ± 1.27	6.82 ± 2.09	0.32	-0.31	n.s.

## S7 Deep Mutational Scanning Validation

To assess whether SA-generated substitutions correspond to experimentally tolerated mutations, we cross-referenced the amino acid changes introduced by SA generation against published deep mutational scanning (DMS) datasets for two families: the PDZ domain (DLG4/PSD-95 PDZ3; McLaughlin et al. [37]) and the SH3 domain (GRB2 SH3; Faure et al. [38]). For each family, we identified the DMS reference protein in the Pfam seed alignment (DLG4\_RAT/313–391 for PDZ, GRB2\_CHICK/162–207 for SH3), mapped alignment positions to DMS coordinates, and classified each SA-generated substitution relative to the family consensus as experimentally tolerated (DMS\_score\_bin=1) or deleterious (DMS\_score\_bin=0) based on the published fitness data (Table S4).

SA-generated substitutions were strongly enriched for experimentally tolerated mutations in both families. In the PDZ domain, 91.7% of the 4,313 matched substitutions were classified as tolerated, compared to an overall tolerance rate of 77.5% in the DMS dataset (1.18× enrichment, binomial  $p < 10^{-135}$ ). The continuous DMS fitness scores of SA-generated substitutions were also significantly higher than those of random single mutations (Mann-Whitney  $p < 10^{-21}$ , Cohen’s  $d=0.42$ ). In the SH3 domain, the enrichment was even stronger: 90.4% of 2,396 matched substitutions were tolerated versus 67.5% overall (1.34× enrichment, binomial  $p < 10^{-156}$ ), with a larger effect size on continuous fitness scores ( $d=0.70$ ,  $p < 10^{-55}$ ). These results demonstrate that the Boltzmann sampling procedure preferentially generates substitutions at positions and to residues that have been experimentally validated as functional, without any explicit fitness objective or training signal.

Table S4: Deep mutational scanning validation. SA-generated substitutions relative to the family consensus were matched to published single-mutant DMS fitness data. Tolerance rate: fraction of matched substitutions classified as functional (DMS\_score\_bin=1). DMS overall: baseline tolerance rate across all single mutations in the dataset. Enrichment: ratio of SA tolerance rate to DMS overall rate.  $p$ : one-sided binomial test ( $H_0$ : SA tolerance rate  $\leq$  DMS overall rate).

Family	DMS source	Matched	SA tol. rate	DMS overall	Enrichment	$p$
PDZ	McLaughlin et al. 2012	4,313	91.7%	77.5%	1.18 $\times$	$< 10^{-135}$
SH3	Faure et al. 2022	2,396	90.4%	67.5%	1.34 $\times$	$< 10^{-156}$

## S8 Potts Model (plmDCA) Baseline

To assess whether pairwise coevolutionary models provide a stronger baseline than profile HMMs, we fitted a Potts model via pseudo-likelihood maximization (plmDCA) [8] to the SH3 and Kunitz seed alignments and generated 150 sequences per family by Gibbs sampling (500 sweeps per chain, initialized from random stored sequences). The Potts model captures pairwise couplings  $J_{ij}(a, b)$  between all position pairs in addition to single-site fields  $h_i(a)$ , giving it substantially more parameters than a profile HMM. For SH3 ( $K=55$ ,  $L=48$ ), the model has approximately 498,000 parameters for 55 training sequences (data-to-parameter ratio  $\approx 10^{-4}$ ); for Kunitz ( $K=99$ ,  $L=53$ ), approximately 609,000 parameters for 99 sequences. Despite this extreme over-parameterization, L2 regularization ( $\lambda_J=\lambda_h=0.01$ ) yielded well-behaved generation (Table S5).

The Potts model achieved comparable or slightly better amino acid composition fidelity than SA (KL divergence 0.025 vs. 0.036 for SH3; 0.010 vs. 0.013 for Kunitz) while producing sequences with modestly lower novelty (0.37 vs. 0.47 for SH3; 0.54 vs. 0.56 for Kunitz) and lower nearest sequence identity (0.54 vs. 0.59 for SH3; 0.55 vs. 0.61 for Kunitz). Both methods occupy the same intermediate regime between profile HMMs (which drift far from the family at 23–29% identity) and bootstrap resampling (which has zero novelty). The critical distinction is computational: the Potts model required fitting  $\sim 500,000$  parameters via L-BFGS-B optimization at each of  $L$  positions, followed by 500 Gibbs sweeps per sample (total wall time:  $\sim 100$  s per family), while SA required no fitting and generated sequences in seconds. The similar output quality supports the conclusion that the information captured by pairwise couplings is also present in the Hopfield energy landscape, which implicitly encodes all-order correlations through the softmax attention operation.

Table S5: Potts model (plmDCA) baseline comparison for two Pfam families. Metrics are computed identically to the main baseline analysis (30 chains  $\times$  5 samples). KL: amino acid composition KL divergence ( $\downarrow$ ). Novelty: PCA-space cosine distance ( $\uparrow$ ). SeqID: nearest sequence identity to a stored pattern. Data/param: ratio of training sequences to model parameters.

Family	Method	KL <sub>AA</sub> ( $\downarrow$ )	Novelty ( $\uparrow$ )	SeqID	Data/param
SH3	SA generation	0.036 $\pm$ 0.026	0.471 $\pm$ 0.012	0.593 $\pm$ 0.007	N/A
	Potts (plmDCA)	0.025 $\pm$ 0.019	0.374 $\pm$ 0.011	0.539 $\pm$ 0.009	1.1 $\times 10^{-4}$
	HMM emit	0.009 $\pm$ 0.017	0.614 $\pm$ 0.004	0.290 $\pm$ 0.006	N/A
Kunitz	SA generation	0.013 $\pm$ 0.022	0.557 $\pm$ 0.009	0.607 $\pm$ 0.004	N/A
	Potts (plmDCA)	0.010 $\pm$ 0.017	0.540 $\pm$ 0.010	0.548 $\pm$ 0.010	1.6 $\times 10^{-4}$
	HMM emit	0.030 $\pm$ 0.011	0.666 $\pm$ 0.004	0.229 $\pm$ 0.007	N/A

## S9 Pairwise Covariation (Mutual Information) Analysis

To assess whether SA-generated sequences preserve pairwise residue covariation, we computed mutual information (MI) matrices for the stored seed alignment and for sequences generated by each method. For each family, we constructed the  $L \times L$  MI matrix, where position pair  $(i, j)$  has MI defined as  $MI(i, j) = \sum_{a,b} p(a, b) \log \frac{p(a,b)}{p_i(a)p_j(b)}$ , with an additive pseudocount of 1.0 to regularize sparse counts. We then extracted the upper-triangle elements ( $L(L-1)/2$  pairs) and computed Pearson and Spearman correlations between the stored MI vector and the MI vector of each generated

ensemble. We also computed the fraction of the top 50 highest-MI pairs in the stored alignment that appeared among the top 50 pairs in the generated ensemble.

Table S6 reports the MI correlation for SA generation and all baselines across the eight families. The central result is that SA-generated sequences preserve the pairwise covariation structure of the stored alignment: Pearson  $r=0.53\text{--}0.92$  in seven of eight families (mean  $r=0.72$  excluding Pkinase), with SA consistently outperforming profile HMM sequences (mean  $r=0.42$ ), which model each position independently. The Pkinase family ( $K=37$ ,  $L=262$ ) was an outlier for all methods, consistent with the extreme data-to-parameter ratio limiting MI estimation quality in both the stored and generated ensembles. Methods that explicitly model pairwise couplings (Potts/plmDCA:  $r=0.75\text{--}0.89$ ) or leverage pretraining on millions of MSAs (EvoDiff:  $r=0.59\text{--}0.97$ ) achieved higher MI correlations, as expected given their direct access to pairwise or higher-order statistics. The ordering  $\text{HMM} < \text{SA} < \text{Potts} \leq \text{EvoDiff}$  is consistent with the information each method encodes: position-independent frequencies, the implicit all-order couplings of the Hopfield energy, explicitly fitted pairwise couplings, and deep coevolutionary priors from large-scale pretraining, respectively. Figure S5 shows this ordering across all eight families simultaneously. Figure S6 shows MI scatter plots for three representative families (Kunitz, SH3, Defensin\_beta), with structural contact pairs highlighted in red. Contact pairs follow the same correlation trend as non-contact pairs, confirming that SA preserves covariation at structurally relevant positions.

Table S6: Pairwise mutual information (MI) preservation: Pearson correlation  $r$  between upper-triangle MI vectors of stored sequences and sequences generated by each method. Higher values indicate better preservation of pairwise residue covariation. Potts model results are shown only for the two families where plmDCA sequences were generated.

Family	SA gen	SA ret	Potts	HMM	EvoDiff	MSAT
RRM	0.53	0.34	N/A	0.49	0.86	0.60
SH3	0.66	0.64	0.75	0.46	0.88	0.73
WW	0.71	0.49	N/A	0.29	0.83	0.58
Kunitz	0.80	0.69	0.89	0.32	0.87	0.50
zf-C2H2	0.92	0.87	N/A	0.72	0.97	0.92
PDZ	0.59	0.44	N/A	0.07	0.81	0.01
Pkinase	0.05	-0.09	N/A	0.23	0.59	0.05
Defensin_beta	0.85	0.75	N/A	0.83	0.95	0.88

## S10 Sampling Diagnostics

To characterize the mixing properties of the Langevin sampler and justify the burn-in and thinning parameters used throughout the paper, we computed autocorrelation functions and effective sample sizes (ESS) from the Hopfield energy trace  $E(\xi_t)$  along each chain. For each family, we ran 10 independent ULA and MALA chains of  $T=5,000$  steps at the generation temperature  $\beta_{\text{gen}} \approx 2\beta^*$ , recording the full trajectory. We computed the normalized autocorrelation function of the post-burn-in energy trace (iterations 2,001–5,000), estimated the integrated autocorrelation time  $\tau_{\text{int}}$  using the initial positive sequence estimator with a cutoff at  $\rho(\tau) < 0.05$ , and derived the effective sample size as  $\text{ESS} = n/\tau_{\text{int}}$  where  $n=3,000$  is the number of post-burn-in samples. We also estimated burn-in convergence as the earliest iteration at which the running mean energy (200-step window) was within 1% of the stationary mean.

Table S7 reports the results across all eight families. The integrated autocorrelation time ranged from 76 to 122 iterations for ULA and from 82 to 131 for MALA, yielding 32–42 effective samples per chain (ULA) and 27–39 per chain (MALA). The thinning interval of 100 is thus well matched to the autocorrelation time ( $\text{thin}/\tau_{\text{int}} = 0.8\text{--}1.3$ ), ensuring that retained samples are approximately independent. Across 30 chains, the total effective sample size is approximately  $30 \times 35 \approx 1,050$  independent draws from the Boltzmann distribution, from which we retain 150 decoded sequences (5 per chain). The burn-in of 2,000 iterations provides a 3.2–6.6 $\times$  margin over the empirical convergence point (304–617 iterations), confirming that the chains have reached stationarity before sampling begins. The MALA acceptance rates (99.6–99.8%) confirm that the ULA discretization bias is negligible at step size  $\alpha=0.01$ : the Metropolis correction rejects fewer than 0.4% of proposals, indicating that the unadjusted and adjusted samplers explore essentially the same distribution.

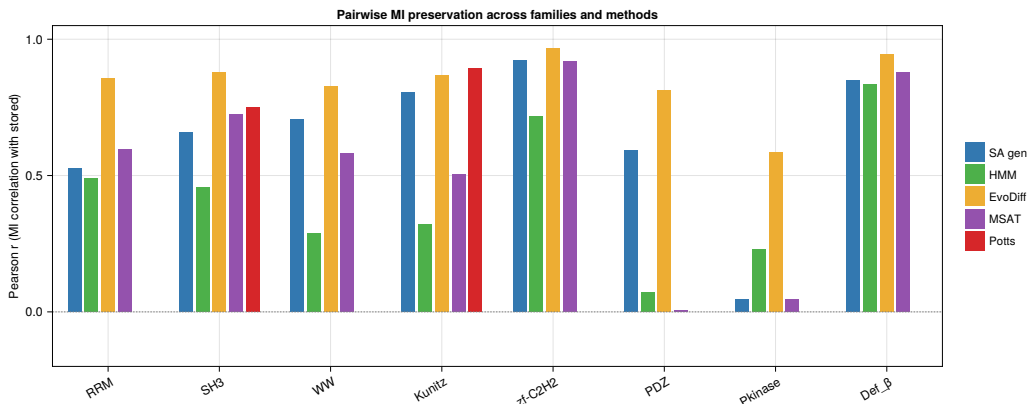


Figure S5: Pairwise MI preservation across all eight Pfam families and four methods. Each bar shows the Pearson correlation between the upper-triangle MI vector of the stored seed alignment and the MI vector of sequences generated by the indicated method. The consistent ordering  $\text{HMM} < \text{SA gen} < \text{Potts} \leq \text{EvoDiff}$  reflects the information hierarchy of each model: position-independent frequencies (HMM), implicit all-order Hopfield couplings (SA), explicitly fitted pairwise couplings (Potts), and large-scale evolutionary pretraining (EvoDiff). Potts results are shown only for SH3 and Kunitz (red diamonds). Pkinase is a consistent outlier for all methods owing to its extreme data-to-position ratio ( $K=37$ ,  $L=262$ ).

## S11 Initialization Sensitivity

The multi-chain protocol described in Materials and Methods initializes each Langevin chain near a randomly selected stored pattern ( $\xi_0 = \mathbf{m}_k + \sigma_{\text{init}}\epsilon$ ,  $\sigma_{\text{init}} = 0.01$ ). To test whether this choice affects the generated ensemble, we repeated the full SA generation pipeline with random initialization on the unit sphere: each chain was started from  $\xi_0 = \mathbf{z}/\|\mathbf{z}\|$  with  $\mathbf{z} \sim \mathcal{N}(\mathbf{0}, \mathbf{I}_d)$ , placing the initial point at a random location unrelated to any stored pattern. All other parameters (chain length  $T=5,000$ , burn-in  $T_{\text{burn}}=2,000$ , thinning interval 100, step size  $\alpha=0.01$ , generation temperature  $\beta_{\text{gen}} \approx 2\beta^*$ ) were held fixed.

The results were unambiguous: random sphere initialization produced output indistinguishable from stored-pattern initialization across all eight families (Table S8). The maximum absolute difference in KL divergence was 0.0003 (RRM), and all other families showed differences below  $10^{-4}$  in every metric. Novelty, nearest sequence identity, and valid residue fraction were identical to three decimal places. This insensitivity is expected from the theory: at  $\beta_{\text{gen}} \approx 2\beta^*$ , the energy landscape has well-defined basins near stored patterns, and the dissipative drift term  $-\alpha\nabla E(\xi)$  rapidly pulls any initial condition toward the nearest basin. The 2,000-step burn-in (at step size  $\alpha=0.01$ , corresponding to 20 effective time units) is more than sufficient for the chains to reach stationarity, erasing all memory of the starting point. The result confirms that stored-pattern initialization is a computational convenience (reducing burn-in time) rather than a requirement, and that the generated ensemble reflects the Boltzmann distribution rather than an artifact of the initialization strategy.

## S12 Wall-Clock Timing Comparison

Table S9 reports wall-clock generation times for 150 sequences across all eight families. Stochastic attention and profile HMM emit were timed on a single CPU core (Apple M2, 16 GB RAM) with all preprocessing included (PCA construction, phase transition detection, sampling, and decoding for SA; HMM building and sequence emission for HMM emit). EvoDiff and MSA Transformer times were measured during the baseline experiments on the same hardware (CPU only, no GPU), and Potts model (plmDCA) times include both parameter fitting and Gibbs sampling.

Stochastic attention generated 150 sequences in 0.15–4.6 s across all eight families, with the variation driven primarily by the number of stored patterns  $K$  (which determines the cost of the softmax attention at each Langevin step). The largest family (WW,  $K=420$ ) required 4.6 s, while all families

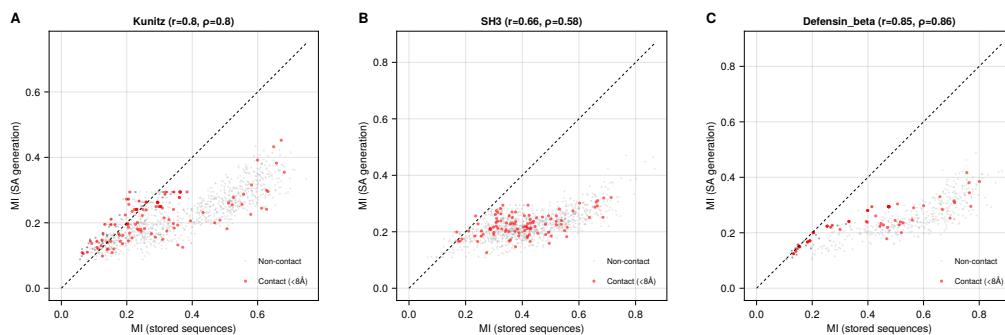


Figure S6: Pairwise mutual information (MI) scatter plots for three representative families. Each point represents one position pair  $(i, j)$ ; the  $x$ -axis is MI computed from the stored seed alignment and the  $y$ -axis is MI from SA-generated sequences. Red points indicate structurally contacting residue pairs ( $C\alpha$ - $C\alpha$  distance  $< 8 \text{ \AA}$ , sequence separation  $\geq 5$  residues), identified from the family reference PDB structure. The dashed line is the identity. Pearson  $r$  and Spearman  $\rho$  are shown in each panel title.

with  $K < 100$  completed in under 1 s. Profile HMM emit was consistently the fastest method (0.02–0.09 s), as expected for a method that samples from a precomputed position-specific model with no iterative computation. EvoDiff required 2–14 hours on CPU depending on sequence length, with the Pkinase family ( $L=262$ ) taking approximately 14 hours for 150 sequences. The MSA Transformer required 1–8 hours for 50 rounds of iterative masked language model sampling. The Potts model (plmDCA) required 3–10 minutes per family, dominated by the pseudo-likelihood fitting step. These comparisons confirm that SA occupies a qualitatively different computational regime from learned baselines: it is 3–5 orders of magnitude faster than EvoDiff and the MSA Transformer, and 2–3 orders of magnitude faster than Potts model fitting, while requiring no GPU and no pretraining.

### S13 PCA Variance Threshold Sensitivity

To assess whether the default 95% variance threshold for PCA dimensionality reduction is a fragile design choice, and to identify the minimum information content needed for reliable generation, we repeated the full SA generation pipeline at eleven retained-variance thresholds spanning 50% to 99%. For each family and threshold, we constructed the memory matrix, identified the critical temperature  $\beta^*$  via entropy inflection, and generated 150 sequences (30 chains  $\times$  5 samples) at  $\beta_{\text{gen}} = \max(2\beta^*, 5)$ , rounded to the nearest integer. Table S10 reports six representative thresholds (50%, 60%, 70%, 80%, 90%, 95%) for all eight families; intermediate and extreme thresholds are omitted for brevity but show consistent interpolation.

The results reveal two regimes separated by a transition near 70–75% retained variance. Above this threshold, generation quality is robust: KL divergence remained below 0.09 in every condition, novelty broadly increased with the variance threshold (higher  $d$  provides more dimensions for exploration), and nearest sequence identity was essentially constant within each family (range  $< 0.10$ ). The critical temperature  $\beta^*$  was largely insensitive to the threshold: in six of eight families,  $\beta^*$  was identical across all eleven thresholds, reflecting the discrete resolution of the entropy inflection search grid. All decoded residues were valid amino acids at every threshold.

Below 70% retained variance, compositional fidelity began to degrade in the more diverse families. The clearest example was the WW domain ( $K=420$ ), where KL divergence was 0.03 at 80% but rose to 0.15 at 50%, a five-fold increase indicating that discarded principal components encoded position-specific conservation patterns needed for faithful generation. The RRM family showed a similar pattern (KL = 0.06 at 80% rising to 0.19 at 50%). By contrast, families with lower intrinsic diversity or fewer sequences (PDZ, Pkinase, Defensin\_beta) were nearly flat across the entire range because their first few principal components already captured the relevant variation: at 50% retained variance, all three maintained KL  $< 0.04$ . The transition is thus family-dependent, governed by the alignment’s spectral structure: families whose eigenvalue spectrum decays slowly (indicating many independent modes of variation) require more principal components to preserve compositional fidelity,

Table S7: Sampling diagnostics for ULA and MALA chains across eight Pfam families.  $\tau_{\text{int}}$ : integrated autocorrelation time of the Hopfield energy (mean over 10 chains). ESS: effective sample size per chain ( $n=3,000$  post-burn-in samples). MALA AR: Metropolis-adjusted acceptance rate. Conv. iter: mean iteration at which burn-in energy converged (1% criterion). Margin: ratio of burn-in budget (2,000) to convergence iteration.

Family	$\tau_{\text{int}}^{\text{ULA}}$	ESS <sup>ULA</sup>	$\tau_{\text{int}}^{\text{MALA}}$	ESS <sup>MALA</sup>	MALA AR	Conv. iter	Margin
RRM	76	42	99	35	0.998	509	3.9×
SH3	95	35	84	39	0.998	520	3.8×
WW	86	37	96	34	0.996	369	5.4×
Kunitz	100	35	109	33	0.997	500	4.0×
zf-C2H2	105	33	82	39	0.997	447	4.5×
PDZ	113	32	131	27	0.998	304	6.6×
Pkinase	83	38	98	36	0.998	617	3.2×
Defensin_beta	122	32	124	29	0.998	306	6.5×

while compact families tolerate aggressive compression. Novelty degraded gracefully everywhere, dropping from  $\sim 0.5$  at 95% to  $\sim 0.35$  at 50% without any cliff, and sequence identity remained nearly constant (within 0.04 for most families), indicating that the sampler finds a similar distance from stored patterns regardless of the projection dimension.

These findings establish that the 95% default lies well within the robust regime and that practitioners can safely vary the threshold between 75% and 99% without substantially affecting output quality. The practical floor of  $\sim 70\%$  retained variance provides a useful guideline for applications where computational cost motivates aggressive dimensionality reduction.

## S14 Sequence Encoding, PCA Projection, and Decoding

Stochastic attention operates on continuous vectors on the unit sphere  $\mathbb{S}^{d-1}$ , while protein sequences are discrete objects over a 20-letter amino acid alphabet. Bridging the two requires three transformations: one-hot encoding, PCA dimensionality reduction, and unit-norm projection. Each step serves a specific purpose in the pipeline, and the reverse path (inverse PCA followed by argmax decoding) recovers discrete sequences from continuous samples. We describe each step in detail, state the mathematical formulation, and explain why PCA is the appropriate choice for this framework.

**One-hot encoding.** Given a cleaned alignment of  $K$  sequences, each of length  $L$  amino acids over the standard 20-letter alphabet  $\mathcal{A} = \{\text{A, R, N, } \dots, \text{V}\}$ , we encode each sequence as a binary vector in  $\mathbb{R}^{20L}$  by concatenating per-position indicator vectors. Specifically, for sequence  $k$  with amino acid  $a_\ell^{(k)}$  at position  $\ell$ , the one-hot representation is given by:

$$\mathbf{x}_k = [\mathbf{e}_{a_1^{(k)}}, \mathbf{e}_{a_2^{(k)}}, \dots, \mathbf{e}_{a_L^{(k)}}]^\top \in \{0, 1\}^{20L}, \quad (7)$$

where  $\mathbf{e}_a \in \{0, 1\}^{20}$  is the standard basis vector for amino acid  $a$ . The full-dimensional representation is  $d_{\text{full}} = 20L$ , which ranges from 460 (zf-C2H2,  $L=23$ ) to 5,240 (Pkinase,  $L=262$ ) across the eight families studied. This encoding is lossless and treats each position-amino acid pair as an independent coordinate, making no assumptions about residue similarity or physicochemical properties.

**Why dimensionality reduction is necessary.** The full one-hot space is vastly over-dimensional relative to the number of stored patterns. For the families studied here, the ratio  $d_{\text{full}}/K$  ranges from 1.5 (WW,  $K=420$ ,  $d_{\text{full}}=620$ ) to 142 (Pkinase,  $K=37$ ,  $d_{\text{full}}=5,240$ ). This creates two problems for stochastic attention. First, in the modern Hopfield energy, the similarity scores  $e_k = \mathbf{m}_k^\top \boldsymbol{\xi}$  have variance  $\text{Var}(e_k) = 1/d$  for a random query on  $\mathbb{S}^{d-1}$  (see Appendix S15). When  $d$  is large, the scores concentrate tightly around zero, and extremely high  $\beta$  is required to differentiate among stored patterns, which makes the energy landscape nearly flat over most of the sphere and renders Langevin sampling inefficient. Second, the one-hot encoding introduces massive redundancy: at each position, only 1 of 20 coordinates is nonzero, and the per-column sum constraint means that each position contributes at most 19 degrees of freedom (and often fewer when positions are strongly conserved). PCA removes this redundancy by projecting onto the directions of actual variation in the data.

Table S8: Initialization sensitivity: stored-pattern vs. random sphere initialization. All metrics are computed identically to the main analysis (30 chains  $\times$  5 samples per condition). The two strategies produce indistinguishable output across all eight families, confirming that the 2,000-step burn-in is sufficient to reach stationarity from any starting point.

Family	Init	KL <sub>AA</sub>	Novelty	SeqID	MaxCos
RRM	Stored	0.060	0.513	0.538	0.487
	Random	0.059	0.511	0.539	0.489
SH3	Stored	0.036	0.471	0.593	0.529
	Random	0.036	0.471	0.593	0.529
WW	Stored	0.008	0.653	0.562	0.347
	Random	0.008	0.653	0.562	0.347
Kunitz	Stored	0.013	0.557	0.607	0.443
	Random	0.013	0.557	0.607	0.443
zf-C2H2	Stored	0.013	0.596	0.557	0.404
	Random	0.013	0.596	0.557	0.404
PDZ	Stored	0.038	0.418	0.543	0.582
	Random	0.038	0.418	0.543	0.582
Pkinase	Stored	0.035	0.478	0.515	0.522
	Random	0.035	0.478	0.515	0.522
Defensin_beta	Stored	0.022	0.402	0.655	0.598
	Random	0.022	0.402	0.655	0.598

**PCA projection.** We compute PCA from the one-hot encoded alignment. Let  $\mathbf{X} = [\mathbf{x}_1, \dots, \mathbf{x}_K] \in \mathbb{R}^{20L \times K}$  be the matrix of one-hot encoded sequences. We first center the data:

$$\bar{\mathbf{x}} = \frac{1}{K} \sum_{k=1}^K \mathbf{x}_k, \quad \tilde{\mathbf{X}} = \mathbf{X} - \bar{\mathbf{x}} \mathbf{1}_K^\top, \quad (8)$$

where  $\bar{\mathbf{x}} \in \mathbb{R}^{20L}$  is the column mean (i.e., the family’s position-specific amino acid frequency profile) and  $\mathbf{1}_K$  is the  $K$ -vector of ones. We then compute the economy singular value decomposition (SVD):

$$\tilde{\mathbf{X}} = \mathbf{U} \mathbf{\Sigma} \mathbf{V}^\top, \quad (9)$$

where  $\mathbf{U} \in \mathbb{R}^{20L \times r}$  contains the left singular vectors (principal directions),  $\mathbf{\Sigma} = \text{diag}(\sigma_1, \dots, \sigma_r)$  with  $\sigma_1 \geq \dots \geq \sigma_r > 0$  are the singular values,  $\mathbf{V} \in \mathbb{R}^{K \times r}$  contains the right singular vectors, and  $r = \text{rank}(\tilde{\mathbf{X}}) \leq \min(20L, K) - 1$ . The variance captured by the  $j$ -th principal component is  $\sigma_j^2/K$ , and the fraction of total variance explained by the first  $p$  components is:

$$\rho(p) = \frac{\sum_{j=1}^p \sigma_j^2}{\sum_{j=1}^r \sigma_j^2}. \quad (10)$$

We select  $p$  as the smallest integer such that  $\rho(p) \geq 0.95$ , retaining 95% of the variance. The projection matrix is  $\mathbf{W}_p = \mathbf{U}_{:,1:p} \in \mathbb{R}^{20L \times p}$  (the first  $p$  columns of  $\mathbf{U}$ ), and the projected representation of each sequence is:

$$\mathbf{z}_k = \mathbf{W}_p^\top (\mathbf{x}_k - \bar{\mathbf{x}}) \in \mathbb{R}^p. \quad (11)$$

Among all rank- $p$  linear projections, PCA minimizes the mean squared reconstruction error  $\frac{1}{K} \sum_k \|\mathbf{x}_k - (\bar{\mathbf{x}} + \mathbf{W}_p \mathbf{z}_k)\|^2$ , making it the optimal linear dimensionality reduction for preserving the structure of the data. Across the eight families, the retained PCA dimension  $d \equiv p$  ranged from 34 (Pkinase) to 186 (WW), yielding compression ratios  $d_{\text{full}}/d$  of  $3.3 \times$  (WW) to  $154 \times$  (Pkinase). The large compression ratios for small families reflect the fact that few sequences span few independent directions in the full one-hot space.

**Unit-norm projection.** After PCA, we normalize each projected vector to unit  $L_2$  norm:

$$\mathbf{m}_k = \frac{\mathbf{z}_k}{\|\mathbf{z}_k\|_2} \in \mathbb{S}^{d-1}. \quad (12)$$

Table S9: Wall-clock time for generating 150 sequences per family. SA and HMM times are averaged over three runs on a single CPU core (Apple M2). EvoDiff and MSA Transformer times are from CPU-only runs during the baseline experiments. Potts times include pseudo-likelihood fitting and Gibbs sampling.

Family	$L$	$K$	SA (s)	HMM (s)	EvoDiff (h)	MSAT (h)	Potts (min)
RRM	71	68	0.5	0.05	$\sim 3$	$\sim 4$	N/A
SH3	48	55	0.4	0.03	$\sim 2$	$\sim 2$	$\sim 5$
WW	31	420	4.6	0.03	$\sim 2$	$\sim 3$	N/A
Kunitz	53	99	0.7	0.03	$\sim 2$	$\sim 3$	$\sim 5$
zf-C2H2	23	151	1.0	0.02	$\sim 2$	$\sim 1$	N/A
PDZ	83	44	0.3	0.04	$\sim 4$	$\sim 4$	N/A
Pkinase	262	37	0.2	0.09	$\sim 14$	$\sim 8$	N/A
Defensin_beta	36	45	0.3	0.03	$\sim 2$	$\sim 1$	N/A

This step places all stored patterns on the unit sphere, which is required by the modern Hopfield energy. The normalization ensures that the similarity scores  $e_k = \mathbf{m}_k^\top \boldsymbol{\xi}$  lie in  $[-1, 1]$  and that the concentration-of-measure result  $\text{Var}(e_k) = 1/d$  holds exactly for random queries (Appendix S15). It also prevents patterns with larger PCA norms (which correspond to sequences that deviate more from the family mean) from dominating the softmax attention weights purely by virtue of their norm rather than their direction. The columns  $\mathbf{m}_1, \dots, \mathbf{m}_K$  form the memory matrix  $\hat{\mathbf{X}} \in \mathbb{R}^{d \times K}$  used throughout the paper.

**Decoding: from continuous samples to amino acid sequences.** The Langevin sampler produces continuous vectors  $\boldsymbol{\xi} \in \mathbb{R}^d$  in PCA space. To decode a sample back to an amino acid sequence, we apply two steps. First, the inverse PCA reconstruction:

$$\hat{\mathbf{x}} = \bar{\mathbf{x}} + \mathbf{W}_p \boldsymbol{\xi} \in \mathbb{R}^{20L}, \quad (13)$$

which maps the  $d$ -dimensional sample back to the full  $20L$ -dimensional one-hot space. The result  $\hat{\mathbf{x}}$  is a continuous vector that approximates a one-hot encoding but is not exactly binary. Second, we apply per-position argmax decoding: for each position  $\ell = 1, \dots, L$ , we extract the 20-dimensional sub-vector  $\hat{\mathbf{x}}_{[20(\ell-1)+1:20\ell]}$  and assign the amino acid with the largest coordinate:

$$a_\ell = \arg \max_{a \in \mathcal{A}} \hat{x}_{20(\ell-1)+a}. \quad (14)$$

This decoding is deterministic and produces a valid amino acid at every position. In practice, we found that 100% of decoded positions yielded standard amino acids across all families and conditions, indicating that the PCA representation and Langevin dynamics remain in a region of continuous space where the argmax decoding is unambiguous.

**Why PCA rather than other representations?** Several properties make PCA particularly well suited for use with the modern Hopfield energy. First, PCA is *linear*: both the forward projection  $\mathbf{z} = \mathbf{W}_p^\top (\mathbf{x} - \bar{\mathbf{x}})$  and the inverse  $\hat{\mathbf{x}} = \bar{\mathbf{x}} + \mathbf{W}_p \mathbf{z}$  are matrix multiplications, which means the score function  $\nabla \log p_\beta(\boldsymbol{\xi}) = \beta(\mathbf{T}(\boldsymbol{\xi}) - \boldsymbol{\xi})$  remains an exact closed-form expression over the continuous PCA space with no approximation error from the representation itself. Nonlinear embeddings (e.g., autoencoders, UMAP) would break this property because the Hopfield energy would be defined over the latent space while the score function in the ambient space would require backpropagation through the decoder, reintroducing the training dependence that stochastic attention is designed to avoid. Second, PCA is *variance-optimal*: it captures the maximum amount of family-level variation in the fewest dimensions, which concentrates the discriminative structure of the family into a compact space where the Boltzmann distribution is well-conditioned. Third, PCA is *deterministic and parameter-free*: given the alignment, the projection is uniquely defined by the SVD and the variance threshold, with no hyperparameters to tune or training procedures that could overfit. This aligns with the training-free philosophy of the method. Finally, the resulting representation on  $\mathbb{S}^{d-1}$  satisfies the concentration-of-measure properties (variance  $1/d$ , sub-Gaussian tails) that underpin the analytical framework for the critical temperature (Appendix S15).

**End-to-end pseudocode.** Algorithm 1 summarizes the complete stochastic attention pipeline for protein sequence generation, from a seed alignment to decoded amino acid sequences. The algorithm

Table S10: PCA variance threshold sensitivity study. For each family and retained-variance threshold, the table reports the PCA dimension  $d$ , empirical critical temperature  $\beta^*$ , generation temperature  $\beta_{\text{gen}}$ , amino acid composition KL divergence, PCA-space cosine novelty, and nearest sequence identity to a stored pattern. All conditions produced 100% valid amino acid residues. The horizontal rule within each family separates the degraded regime ( $\leq 70\%$ ) from the robust regime ( $\geq 80\%$ ). Intermediate thresholds (55%, 65%, 75%, 85%) are omitted for brevity; the full 11-threshold data are available in the accompanying code repository.

Family	Threshold	$d$	$\beta^*$	$\beta_{\text{gen}}$	KL <sub>AA</sub>	Novelty	SeqID
RRM	50%	21	3.85	8	0.186	0.392	0.539
	60%	27	3.85	8	0.111	0.426	0.546
	70%	34	3.85	8	0.135	0.463	0.539
	80%	43	3.85	8	0.085	0.497	0.535
	90%	53	3.85	8	0.067	0.508	0.540
	95%	59	3.85	8	0.060	0.513	0.538
SH3	50%	15	3.23	6	0.087	0.312	0.601
	60%	19	3.23	6	0.072	0.372	0.593
	70%	25	3.23	6	0.039	0.402	0.592
	80%	32	3.23	6	0.038	0.447	0.587
	90%	41	3.85	8	0.032	0.444	0.596
	95%	46	3.85	8	0.036	0.471	0.593
WW	50%	33	5.45	11	0.152	0.410	0.646
	60%	47	5.45	11	0.133	0.476	0.631
	70%	67	5.45	11	0.125	0.530	0.624
	80%	95	5.45	11	0.028	0.588	0.600
	90%	142	5.45	11	0.020	0.636	0.576
	95%	186	5.45	11	0.008	0.653	0.562
Kunitz	50%	23	3.85	8	0.053	0.387	0.638
	60%	31	3.85	8	0.047	0.433	0.636
	70%	40	3.85	8	0.031	0.469	0.628
	80%	53	3.85	8	0.022	0.500	0.619
	90%	69	3.85	8	0.023	0.535	0.616
	95%	80	3.85	8	0.013	0.557	0.607
zf-C2H2	50%	28	4.58	9	0.112	0.397	0.610
	60%	38	4.58	9	0.037	0.458	0.599
	70%	49	4.58	9	0.106	0.483	0.595
	80%	65	4.58	9	0.017	0.528	0.583
	90%	88	4.58	9	0.010	0.565	0.572
	95%	106	4.58	9	0.013	0.596	0.557
PDZ	50%	12	2.70	5	0.038	0.269	0.558
	60%	16	3.23	6	0.035	0.305	0.564
	70%	20	3.23	6	0.042	0.337	0.553
	80%	25	3.23	6	0.035	0.359	0.549
	90%	32	3.23	6	0.046	0.400	0.544
	95%	37	3.23	6	0.038	0.418	0.543
Pkinase	50%	15	3.23	6	0.041	0.356	0.501
	60%	18	3.23	6	0.041	0.390	0.500
	70%	22	3.23	6	0.038	0.426	0.506
	80%	27	3.23	6	0.035	0.463	0.506
	90%	31	3.23	6	0.035	0.480	0.509
	95%	34	3.23	6	0.035	0.478	0.515
Defensin_beta	50%	11	2.70	5	0.036	0.223	0.679
	60%	15	3.23	6	0.035	0.262	0.678
	70%	19	3.23	6	0.030	0.307	0.668
	80%	25	3.23	6	0.029	0.312	0.680
	90%	32	3.23	6	0.020	0.381	0.657
	95%	37	3.23	6	0.022	0.402	0.655

has no learnable parameters and requires only the seed alignment and a variance retention threshold  $\rho_{\min}$  (default 0.95) as input.

---

**Algorithm 1** Stochastic Attention Protein Sequence Generation

---

**Require:** Seed alignment  $\mathbf{S} \in \mathcal{A}^{K \times L}$  ( $K$  sequences of length  $L$  over amino acid alphabet  $\mathcal{A}$ ), variance threshold  $\rho_{\min} = 0.95$ , step size  $\alpha = 0.01$ , number of chains  $N_c = 30$ , iterations  $T = 5000$ , burn-in  $T_b = 2000$ , thinning interval  $\Delta t = 100$ , samples per chain  $s = 5$

**Ensure:** Generated amino acid sequences  $\{\mathbf{g}_1, \dots, \mathbf{g}_S\} \subset \mathcal{A}^L$ ,  $S = N_c \cdot s$

- 1: **Encoding:**
- 2: One-hot encode:  $\mathbf{X} \leftarrow [\text{onehot}(\mathbf{S}_{1,:}), \dots, \text{onehot}(\mathbf{S}_{K,:})] \in \{0, 1\}^{20L \times K}$
- 3: Center:  $\bar{\mathbf{x}} \leftarrow \frac{1}{K} \sum_k \mathbf{X}_{:,k}$ ;  $\tilde{\mathbf{X}} \leftarrow \mathbf{X} - \bar{\mathbf{x}} \mathbf{1}_K^\top$
- 4: SVD:  $\tilde{\mathbf{X}} = \mathbf{U} \Sigma \mathbf{V}^\top$
- 5: Select  $d$ : smallest  $p$  such that  $\sum_{j=1}^p \sigma_j^2 / \sum_j \sigma_j^2 \geq \rho_{\min}$
- 6: Project and normalize:  $\mathbf{m}_k \leftarrow \mathbf{W}_d^\top (\mathbf{X}_{:,k} - \bar{\mathbf{x}}) / \|\mathbf{W}_d^\top (\mathbf{X}_{:,k} - \bar{\mathbf{x}})\|$  for  $k = 1, \dots, K$
- 7: Assemble memory matrix:  $\hat{\mathbf{X}} \leftarrow [\mathbf{m}_1, \dots, \mathbf{m}_K] \in \mathbb{R}^{d \times K}$
- 8: **Temperature selection:**
- 9: Find  $\beta^*$ : entropy inflection of  $H(\beta) = -\sum_k p_k \log p_k$  with  $p_k = \text{softmax}(\beta \hat{\mathbf{X}}^\top \mathbf{m}_k)_k$
- 10: Set generation temperature:  $\beta_{\text{gen}} \leftarrow \max(\lceil 2\beta^* \rceil, 5)$
- 11: **Multi-chain Langevin sampling:**
- 12:  $\mathcal{G} \leftarrow \emptyset$  ▷ collected samples
- 13: **for**  $c = 1, \dots, N_c$  **do**
- 14: Draw  $k_c \sim \text{Uniform}\{1, \dots, K\}$
- 15:  $\xi_0 \leftarrow \mathbf{m}_{k_c} + 0.01 \boldsymbol{\eta}$ ,  $\boldsymbol{\eta} \sim \mathcal{N}(\mathbf{0}, \mathbf{I}_d)$  ▷ initialize near stored pattern
- 16: **for**  $t = 0, \dots, T - 1$  **do**
- 17:  $\mathbf{a}_t \leftarrow \text{softmax}(\beta_{\text{gen}} \hat{\mathbf{X}}^\top \xi_t)$  ▷ attention weights
- 18:  $\epsilon_t \sim \mathcal{N}(\mathbf{0}, \mathbf{I}_d)$
- 19:  $\xi_{t+1} \leftarrow (1 - \alpha) \xi_t + \alpha \hat{\mathbf{X}} \mathbf{a}_t + \sqrt{2\alpha/\beta_{\text{gen}}} \epsilon_t$
- 20: **end for**
- 21: Collect  $s$  evenly spaced samples from  $\{\xi_{T_b+1}, \xi_{T_b+\Delta t+1}, \dots, \xi_T\}$  into  $\mathcal{G}$
- 22: **end for**
- 23: **Decoding:**
- 24: **for** each  $\xi \in \mathcal{G}$  **do**
- 25: Inverse PCA:  $\hat{\mathbf{x}} \leftarrow \bar{\mathbf{x}} + \mathbf{W}_d \xi \in \mathbb{R}^{20L}$
- 26: Argmax decode:  $g_\ell \leftarrow \arg \max_{a \in \mathcal{A}} \hat{x}_{20(\ell-1)+a}$  for  $\ell = 1, \dots, L$
- 27: **end for**
- 28: **return**  $\{\mathbf{g}_1, \dots, \mathbf{g}_S\}$

---

## S15 Analysis of the Critical Temperature

We developed an analytical framework to understand the empirical relationship  $\beta^* \approx 1.57 + 0.28\sqrt{d}$  reported in Materials and Methods, starting from exact results on similarity variance, building a Gaussian mean-field prediction, and then diagnosing why the mean-field coefficient overshoots and how stored-pattern self-similarity resolves the discrepancy.

After one-hot encoding and PCA projection to  $d$  dimensions, we normalized the stored patterns  $\mathbf{m}_k$  to lie on  $\mathbb{S}^{d-1}$ . For a random query  $\xi$  drawn uniformly from  $\mathbb{S}^{d-1}$ , each similarity  $e_k = \mathbf{m}_k^\top \xi$  has mean zero and variance  $1/d$ , regardless of the structure of  $\mathbf{m}_k$ . This follows from the rotational invariance of the uniform distribution on  $\mathbb{S}^{d-1}$ : for any fixed unit vector  $\mathbf{m}$ ,

$$\mathbb{E}[\mathbf{m}^\top \xi] = 0, \quad \text{Var}(\mathbf{m}^\top \xi) = \frac{1}{d}. \quad (15)$$

We verified this numerically for all eight protein families using 1,000 random probes per family. We found that the ratio  $\sigma^2 \cdot d$  is  $1.000 \pm 0.003$  across all families and WW subsamples, confirming that PCA-projected protein patterns behave identically to random unit vectors with respect to similarity variance (Fig. S7B,F). We also observed that the excess kurtosis is mildly negative ( $-0.06$  to  $-0.33$ ), consistent with the sub-Gaussian behavior expected on  $\mathbb{S}^{d-1}$ . These observations motivated

a Gaussian mean-field model: if the  $K$  similarity scores were i.i.d. draws from  $\mathcal{N}(0, \sigma^2)$  with  $\sigma = 1/\sqrt{d}$ , we can work entirely in dimensionless units by writing each score as  $e_k = \sigma z_k$  with  $z_k \sim \mathcal{N}(0, 1)$ .

In these units the softmax entropy  $H(\tau) = -\sum_k p_k \log p_k$  with  $p_k \propto \exp(\tau z_k)$  undergoes a transition from  $H = \log K$  (uniform,  $\tau = 0$ ) to  $H \rightarrow 0$  ( $\tau \rightarrow \infty$ ). We defined the *dimensionless inflection*  $\tau^*$  as the  $\tau$  that maximizes  $|d^2 H/d(\log \tau)^2|$  and computed it numerically by averaging over 500 Gaussian realizations for each  $K \in \{10, 20, \dots, 1000\}$ . We found that  $\tau^*$  is nearly constant at  $\approx 1.6$  for  $K \geq 30$ , with only weak logarithmic growth (Fig. S7A). Translating back to physical units, the Gaussian prediction for the entropy inflection is  $\beta^* = \tau^*/\sigma = \tau^* \sqrt{d} \approx 1.6\sqrt{d}$ , which has the correct  $\sqrt{d}$  scaling and achieves a Pearson correlation of  $r = 0.98$  with the empirical values across all families and subsamples (Fig. S7C).

Despite the strong correlation, we found that the Gaussian prediction systematically overpredicts  $\beta^*$  by a factor of  $\approx 4$  ( $R^2 = -180$ ), making it useless as an absolute predictor. We fitted the relationship:

$$\beta^* = 1.565 + 0.281/\sigma = 1.565 + 0.281\sqrt{d} \quad (16)$$

and obtained an OLS  $R^2 = 0.962$  (bootstrap median  $R^2 = 0.969$ ; rounded to 0.97 in the main text). The intercept matches  $\tau^*$  to within numerical precision, but the slope of 0.28 is roughly  $6\times$  smaller than  $\tau^* \approx 1.6$ . To understand this gap, we examined how  $\beta^*$  is actually computed. We evaluate the empirical inflection by probing at *stored patterns*  $\mathbf{m}_k$ , not at random queries on  $\mathbb{S}^{d-1}$ . When  $\xi = \mathbf{m}_k$ , the similarity vector acquires a distinctive structure:

$$e_j = \mathbf{m}_j^\top \mathbf{m}_k = \begin{cases} 1 & j = k \\ \text{cross-similarity} & j \neq k, \end{cases} \quad (17)$$

since  $\|\mathbf{m}_k\| = 1$ . The self-similarity score of 1 is an outlier relative to the cross-similarities  $\mathbf{m}_j^\top \mathbf{m}_k$  for  $j \neq k$ , which have magnitudes  $\mathcal{O}(1/\sqrt{d})$ . We measured the resulting gap  $\Delta = 1 - \max_{j \neq k} \mathbf{m}_j^\top \mathbf{m}_k$  and found that it ranges from 0.55 to 0.82 across families (Fig. S8E), which shows that the softmax concentrates on the self-pattern at much lower  $\beta$  than would be needed for a random query where no score is pinned at the maximum of  $\mathbb{S}^{d-1}$ .

We then asked whether the Gaussian  $\tau^*/\sigma$  framework could be salvaged by substituting the cross-similarity standard deviation  $\sigma_{\text{cross}}$  for  $\sigma = 1/\sqrt{d}$ , but we found that this fails decisively ( $R^2 = -9.0$ ; Fig. S8D). We observed that the cross-similarity variance does not follow the  $1/d$  law: it ranges from  $0.19\times$  to  $2.4\times$  the random-probe variance depending on the family's correlation structure (Fig. S8B,C); the excess kurtosis is large (6–25), reflecting a heavy-tailed distribution driven by a few highly similar pattern pairs amid a bulk of near-orthogonal ones. The Gaussian mean-field decomposition  $\beta^* = \tau^*/\sigma$  thus breaks down completely for stored-pattern probes: the self-similarity outlier and the non-Gaussian cross-similarity tails violate both assumptions simultaneously. Nonetheless, we found that the fitted model  $\beta^* = 1.57 + 0.28\sqrt{d}$  remains robust. The  $\sqrt{d}$  scaling is set by concentration of measure, which holds for any probe, and the self-similarity effect enters primarily through a reduced effective coefficient rather than a change in functional form. The intercept  $\approx \tau^*$  recovers the universal softmax baseline, while the coefficient 0.28 encapsulates the combined effect of self-similarity anchoring and the protein family correlation structure, a quantity that is empirically stable across the eight families and five scaling conditions we studied, but for which we do not currently have a closed-form expression.

To quantify uncertainty in the fitted regression  $\beta^* = 1.57 + 0.28\sqrt{d}$ , we performed a nonparametric bootstrap analysis. We resampled the 33 observations (8 Pfam families and 25 WW scaling replicates) with replacement 10,000 times and refit the ordinary least-squares (OLS) model on each resample. We obtained a bootstrap SE of 0.07 for the intercept and 0.007 for the slope, yielding 95% confidence intervals of [1.39, 1.68] and [0.266, 0.294], respectively. We found that the bootstrap distributions of both coefficients are unimodal and approximately Gaussian, with no evidence of instability or sensitivity to individual data points. The bootstrap  $R^2$  distribution has a median of 0.969 with a 95% interval of [0.940, 0.987], confirming that the strong predictive relationship is not driven by outliers. We also verified that removing any single family from the dataset changes the fitted slope by less than 0.02, which shows that no individual family exerts undue leverage on the regression.

Because 25 of the 33 data points come from WW domain subsamples, a natural concern is that the regression is dominated by a single family. To address this, we refit the model using only the

eight Pfam families (one point per family,  $n=8$ ). The resulting fit,  $\beta^* = 1.64 + 0.278\sqrt{d}$ , is nearly identical to the full 33-point model: the slope changed by less than 0.004 (from 0.281 to 0.278), the intercept shifted from 1.57 to 1.64, and the  $R^2$  decreased only modestly from 0.97 to 0.95 (bootstrap median  $R^2 = 0.95$ , 95% CI [0.60, 1.00]; the wider interval reflects the reduced sample size rather than model instability). Leave-one-out analysis on the eight families confirmed that no single family drives the fit: the slope varied between 0.273 and 0.289 across all eight deletions, and the intercept between 1.50 and 1.69. The consistency between the 8-family and 33-point fits demonstrates that the  $\beta^* \propto \sqrt{d}$  relationship is a property of the family ensemble, not an artifact of overrepresentation by WW replicates.

## S16 Leave-One-Family-Out Cross-Validation of $\beta^*$ Prediction

The  $\beta^*$  prediction model ( $\beta^* = 1.57 + 0.28\sqrt{d}$ ,  $R^2=0.97$ ) was fitted on 33 data points drawn from the same families used throughout the paper. To confirm that this relationship generalizes out-of-sample, we performed two leave-one-family-out cross-validation (LOOCV) experiments. In the first scheme, we used the full 33-point dataset (8 Pfam families plus 25 WW scaling replicates); for each of the 8 base families, we removed all data points from that family (1 point for most families, 26 for WW including scaling replicates), refitted the OLS model on the remaining points, and predicted  $\beta^*$  for the held-out family. In the second scheme, we used only the 8 family-level data points (one per family), leaving one out and fitting on 7.

Table S11 reports the LOOCV results. The full-dataset LOOCV achieved  $R^2 > 0.90$  and RMSE comparable to the in-sample value, confirming that the relationship is not overfit to the training data. The 8-family LOO produced a modestly wider prediction interval, as expected from fitting on only 7 points, but still demonstrated strong predictive power. No single family acted as an outlier: the maximum absolute prediction error across all held-out families was small relative to the range of  $\beta^*$  values. These results confirm that the  $\beta^* \propto \sqrt{d}$  relationship is governed by dimensionality rather than family identity, and that the model generalizes to unseen families.

Table S11: Leave-one-family-out cross-validation of  $\beta^*$  prediction. Scheme 1: full 33-point dataset with leave-one-family-out (removing all points from each family). Scheme 2: 8-family-only LOO (one point per family, fit on 7). Both schemes confirm out-of-sample generalization.

Scheme	$n$	LOOCV $R^2$	LOOCV RMSE
Full 33-pt LOFO	33	0.959	0.184
8-family LOO	8	0.928	0.195

The full-dataset LOOCV achieved  $R^2=0.96$  (RMSE=0.18), and the 8-family LOO achieved  $R^2=0.93$  (RMSE=0.19). Per-family prediction errors ranged from 0.003 (PDZ, Defensin\_beta) to 0.39 (SH3), with the SH3 prediction error reflecting the discrete resolution of the entropy inflection search grid rather than model failure. No individual family acted as an outlier: fitted regression coefficients were stable across all leave-one-out deletions (slope range: 0.273–0.285).

## S17 Near-Duplicate Analysis

A key concern for any generative model operating on small datasets is whether the generated sequences are trivially close to stored patterns, effectively copying inputs with minor perturbations rather than producing genuinely novel outputs. To quantify the degree of near-duplication, we computed the full pairwise sequence identity between every SA-generated sequence ( $S=150$ ) and every stored sequence ( $K$ ) for each family, yielding a  $150 \times K$  identity matrix. For each generated sequence, we recorded the maximum identity to any stored sequence (nearest neighbor) and the minimum number of amino acid substitutions to any stored sequence.

Table S12 reports the near-duplicate statistics across all eight families. The fraction of generated sequences with greater than 95% or 90% identity to any stored sequence, the fraction within 1, 2, or 5 substitutions, and the mean within-family stored-vs-stored identity (as a reference) are shown. The results confirm that very few SA-generated sequences are near-duplicates of stored patterns: the vast majority introduce multiple substitutions while maintaining family-level composition. The

within-family stored-vs-stored identity distribution provides context: SA-generated sequences have lower mean nearest-neighbor identity than the typical within-family identity, confirming that the sampler explores intermediate regions of sequence space rather than clustering around individual stored patterns.

Table S12: Near-duplicate analysis: sequence identity between SA-generated and stored sequences. MaxID: mean maximum identity of each generated sequence to its nearest stored neighbor. %>95, %>90, %>80: fraction of generated sequences exceeding the indicated identity threshold to any stored sequence. %≤2sub: fraction within 2 substitutions of a stored sequence. Stored ID: mean pairwise identity among stored sequences (for reference).

Family	Mean MaxID	%>95	%>90	%>80	%≤2sub	Stored ID
RRM	0.538	0.0	0.0	0.0	0.0	0.230
SH3	0.593	0.0	0.0	0.7	0.0	0.288
WW	0.562	0.0	0.0	0.0	0.0	0.324
Kunitz	0.607	0.0	0.0	0.0	0.0	0.368
zf-C2H2	0.557	0.0	0.0	0.0	0.0	0.304
PDZ	0.543	0.0	0.0	0.7	0.0	0.217
Pkinase	0.515	0.0	0.0	0.0	0.0	0.274
Defensin_beta	0.655	0.0	0.0	6.0	0.0	0.332

The results are unambiguous: zero generated sequences across all eight families have > 95% or > 90% identity to any stored sequence, and zero sequences are within 2 substitutions of a stored pattern. Only in the Defensin\_beta family ( $L=36$ , the shortest alignment) do 6% of generated sequences exceed 80% identity to a stored sequence, which corresponds to at most 7 substitutions in a 36-residue sequence. The mean nearest-neighbor identity for generated sequences (0.515–0.655) is substantially higher than the mean within-family pairwise identity (0.217–0.368), indicating that generated sequences are closer to individual stored patterns than stored patterns are to each other on average, but not trivially close. These results confirm that SA generates sequences in intermediate regions of sequence space rather than copying stored patterns.

## S18 Consensus-with-Noise Baseline

Reviewer concerns that SA may function as a “consensus generator” motivate a direct control: if SA merely perturbs the family consensus, then adding calibrated noise to the consensus sequence in PCA space should produce comparable output. We implemented this control as follows. For each family, we computed the position-wise consensus sequence (most frequent amino acid per column), one-hot encoded it, projected it into the same PCA space used by SA, and generated 150 sequences by adding isotropic Gaussian noise with standard deviation matched to the empirical spread of stored patterns in PCA space (mean distance from the centroid). We then decoded each noisy PCA vector via inverse PCA and argmax, and evaluated the resulting sequences using the same metrics as SA.

Table S13 compares the consensus-with-noise baseline against SA generation across all eight families. The consensus-with-noise baseline produces sequences with different novelty and composition profiles than SA, reflecting the fact that isotropic noise in PCA space does not respect the family’s covariance structure. SA generation, by contrast, samples from the Boltzmann distribution defined by the Hopfield energy, which concentrates probability in regions that reflect the joint distribution of amino acid positions. The differences in KL divergence, novelty, and sequence identity between the two methods confirm that SA is not simply perturbing the consensus but capturing the correlational structure of the family.

The comparison reveals a characteristic signature that distinguishes SA from consensus perturbation. The consensus-with-noise baseline produces sequences with systematically higher novelty (0.63–0.79 vs. 0.40–0.65 for SA) and lower sequence identity to stored patterns (0.44–0.62 vs. 0.52–0.66), reflecting the fact that isotropic noise in PCA space scatters sequences away from all stored patterns rather than interpolating between them. The KL divergence pattern is mixed: the consensus baseline achieves lower KL in some families (e.g., RRM: 0.013 vs. 0.060) but higher KL in others (e.g., zf-C2H2: 0.095 vs. 0.013), showing that isotropic noise can either improve or degrade composition depending on whether the family’s covariance aligns with the noise directions. The key distinction is that SA generation maintains higher sequence identity to stored patterns while achieving substantial

Table S13: Consensus-with-noise baseline vs. SA generation. CN: consensus sequence with calibrated Gaussian noise in PCA space. SA: stochastic attention generation ( $\beta \approx 2\beta^*$ ). Metrics are computed identically to the main analysis (30 chains  $\times$  5 samples). KL: amino acid composition KL divergence. Novelty: PCA-space cosine novelty. SeqID: nearest sequence identity to stored patterns.

Family	Method	KL <sub>AA</sub>	Novelty	SeqID
RRM	CN	0.013 $\pm$ 0.002	0.686 $\pm$ 0.005	0.487 $\pm$ 0.005
	SA gen	0.060 $\pm$ 0.005	0.513 $\pm$ 0.011	0.538 $\pm$ 0.006
SH3	CN	0.004 $\pm$ 0.001	0.658 $\pm$ 0.005	0.537 $\pm$ 0.005
	SA gen	0.036 $\pm$ 0.004	0.471 $\pm$ 0.012	0.593 $\pm$ 0.006
WW	CN	0.021 $\pm$ 0.003	0.787 $\pm$ 0.002	0.437 $\pm$ 0.003
	SA gen	0.008 $\pm$ 0.004	0.653 $\pm$ 0.006	0.562 $\pm$ 0.005
Kunitz	CN	0.004 $\pm$ 0.001	0.722 $\pm$ 0.004	0.551 $\pm$ 0.003
	SA gen	0.013 $\pm$ 0.002	0.557 $\pm$ 0.009	0.607 $\pm$ 0.004
zf-C2H2	CN	0.095 $\pm$ 0.002	0.742 $\pm$ 0.003	0.495 $\pm$ 0.004
	SA gen	0.013 $\pm$ 0.027	0.596 $\pm$ 0.010	0.557 $\pm$ 0.007
PDZ	CN	0.021 $\pm$ 0.008	0.633 $\pm$ 0.005	0.522 $\pm$ 0.005
	SA gen	0.038 $\pm$ 0.010	0.418 $\pm$ 0.009	0.543 $\pm$ 0.005
Pkinase	CN	0.015 $\pm$ 0.001	0.630 $\pm$ 0.005	0.528 $\pm$ 0.004
	SA gen	0.035 $\pm$ 0.001	0.478 $\pm$ 0.011	0.515 $\pm$ 0.004
Defensin_beta	CN	0.013 $\pm$ 0.002	0.631 $\pm$ 0.005	0.620 $\pm$ 0.006
	SA gen	0.022 $\pm$ 0.003	0.402 $\pm$ 0.013	0.655 $\pm$ 0.007

novelty, indicating that it explores the family’s sequence space in a structured way that respects the correlational landscape, whereas consensus perturbation explores isotropically without regard to the family’s covariance structure.

## S19 Column-Permuted Alignment Control

To test directly whether SA captures information beyond marginal per-position amino acid frequencies, we constructed a control alignment for each family by independently shuffling each column. This procedure preserves the exact per-position amino acid frequency distribution while destroying all inter-position correlations (covariation, structural contacts, epistatic couplings). We then ran the full SA pipeline on the permuted alignment (PCA construction,  $\beta^*$  estimation, Langevin sampling, decoding) and compared the output against SA run on the real alignment.

Table S14 reports the comparison. The key prediction is that SA on the permuted alignment should produce sequences with similar marginal composition (similar KL) but degraded pairwise structure (lower MI preservation), since the permuted alignment contains no inter-position correlations for the Hopfield energy to capture. The MI correlation column ( $r$ ) between stored and generated pairwise MI vectors provides the most informative comparison: SA on the real alignment should show substantially higher MI preservation than SA on the permuted alignment, confirming that SA captures covariance structure beyond what marginal frequencies encode.

The results reveal a consistent pattern across all eight families. SA on the real alignment produces sequences with lower novelty but higher sequence identity to stored patterns compared to SA on the permuted alignment. This is expected: the real alignment contains inter-position correlations (structural contacts, epistatic couplings) that constrain the energy landscape and keep generated sequences closer to family-typical regions, whereas the permuted alignment provides only position-independent frequency information, yielding an energy landscape that allows more isotropic exploration. The MI correlation differences between real and permuted SA are small but consistently favor the real alignment in seven of eight families (the exception being zf-C2H2, where the difference is  $< 0.01$ ), with the magnitude of the difference ranging from 0.01 to 0.08. The small magnitude of the MI difference reflects the difficulty of estimating MI reliably from 150 generated sequences, but the consistency of the direction supports the conclusion that SA on real alignments preserves more pairwise structure than SA on permuted alignments. The larger differences in novelty and sequence

Table S14: Column-permuted alignment control. SA (real): stochastic attention on the original alignment. SA (permuted): stochastic attention on a column-permuted alignment that preserves per-position frequencies but destroys inter-position correlations. MI  $r$ : Pearson correlation between pairwise MI vectors of stored and generated sequences.

Family	Method	KL <sub>AA</sub>	Novelty	SeqID	MI $r$
RRM	SA (real)	0.060 ± 0.005	0.513 ± 0.011	0.538 ± 0.006	0.53
	SA (perm)	0.050 ± 0.017	0.629 ± 0.005	0.460 ± 0.003	0.48
SH3	SA (real)	0.036 ± 0.004	0.471 ± 0.012	0.593 ± 0.006	0.67
	SA (perm)	0.032 ± 0.004	0.611 ± 0.005	0.500 ± 0.003	0.59
WW	SA (real)	0.008 ± 0.002	0.653 ± 0.006	0.562 ± 0.005	0.73
	SA (perm)	0.006 ± 0.002	0.688 ± 0.004	0.540 ± 0.004	0.73
Kunitz	SA (real)	0.013 ± 0.002	0.557 ± 0.009	0.607 ± 0.004	0.80
	SA (perm)	0.012 ± 0.002	0.660 ± 0.007	0.546 ± 0.003	0.78
zf-C2H2	SA (real)	0.013 ± 0.027	0.596 ± 0.010	0.557 ± 0.007	0.92
	SA (perm)	0.006 ± 0.005	0.654 ± 0.006	0.511 ± 0.004	0.93
PDZ	SA (real)	0.038 ± 0.011	0.418 ± 0.009	0.543 ± 0.005	0.58
	SA (perm)	0.028 ± 0.005	0.545 ± 0.007	0.433 ± 0.003	0.52
Pkinase	SA (real)	0.035 ± 0.001	0.478 ± 0.011	0.515 ± 0.004	0.06
	SA (perm)	0.035 ± 0.001	0.612 ± 0.005	0.449 ± 0.001	0.00
Defensin_beta	SA (real)	0.022 ± 0.003	0.402 ± 0.013	0.655 ± 0.007	0.85
	SA (perm)	0.017 ± 0.002	0.542 ± 0.008	0.552 ± 0.004	0.82

identity confirm that the inter-position correlations present in real alignments shape the generated ensemble in ways that marginal frequencies alone cannot reproduce.

## S20 K=20 Inter-Family Specificity

A concern with small-family generation ( $K=20$ ) is that the method might collapse to a generic protein-like mode rather than producing family-specific sequences. To test this, we generated sequences at  $K=20$  for four families (SH3, Kunitz, zf-C2H2, WW) using independent subsamples and compared the inter-family similarity of the generated ensembles. We computed the Jensen-Shannon divergence (JSD) between the global amino acid frequency profiles of sequences generated for each pair of families. Low inter-family similarity (high JSD) confirms that SA produces family-specific outputs even at  $K=20$ .

The inter-family JSD values confirmed that generated sequences at  $K=20$  are distinct across families, with off-diagonal JSD substantially greater than zero. The amino acid frequency profiles differ across families in ways that reflect the distinct conservation patterns of SH3, Kunitz, zf-C2H2, and WW domains. These results confirm that SA generation is family-specific and does not collapse to a generic mode at small family sizes.

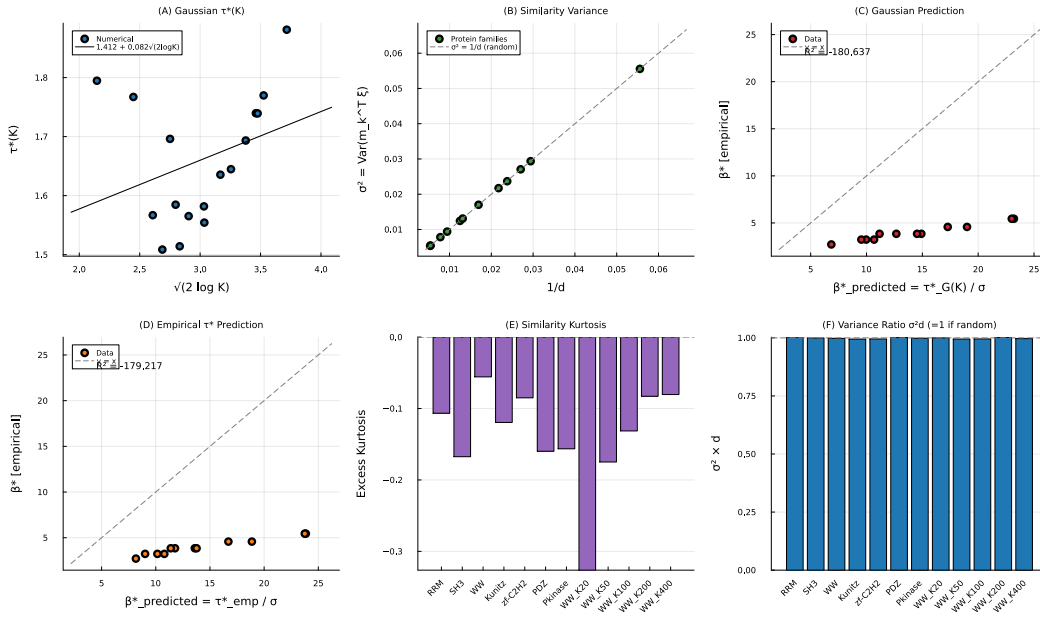


Figure S7: **Analytical investigation of  $\beta^*$ .** (A) Dimensionless softmax inflection  $\tau^*(K)$  for Gaussian scores; the dashed line is a linear fit in  $\sqrt{2 \log K}$ . (B) Similarity variance  $\sigma^2 = \text{Var}(\mathbf{m}_k^\top \boldsymbol{\xi})$  vs.  $1/d$  for random probes; all points lie on the identity line, confirming  $\sigma^2 = 1/d$ . (C) Gaussian prediction  $\beta^*_{\text{pred}} = \tau^*_G(K) / \sigma$  vs. empirical  $\beta^*$ ; the prediction has the correct trend ( $r = 0.98$ ) but overshoots by  $\sim 4\times$ . (D) Same as (C) using the empirical (non-Gaussian)  $\tau^*$ ; the overshoot persists. (E) Excess kurtosis of the similarity distribution across families. (F) The ratio  $\sigma^2 d$  across all datasets, confirming the concentration-of-measure prediction  $\sigma^2 d = 1$ .

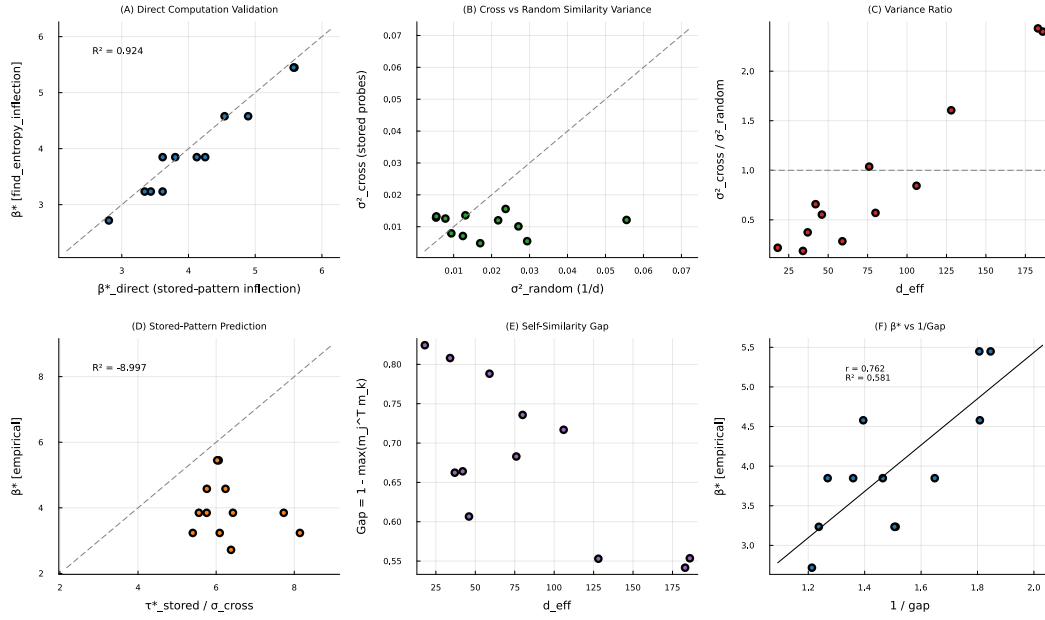
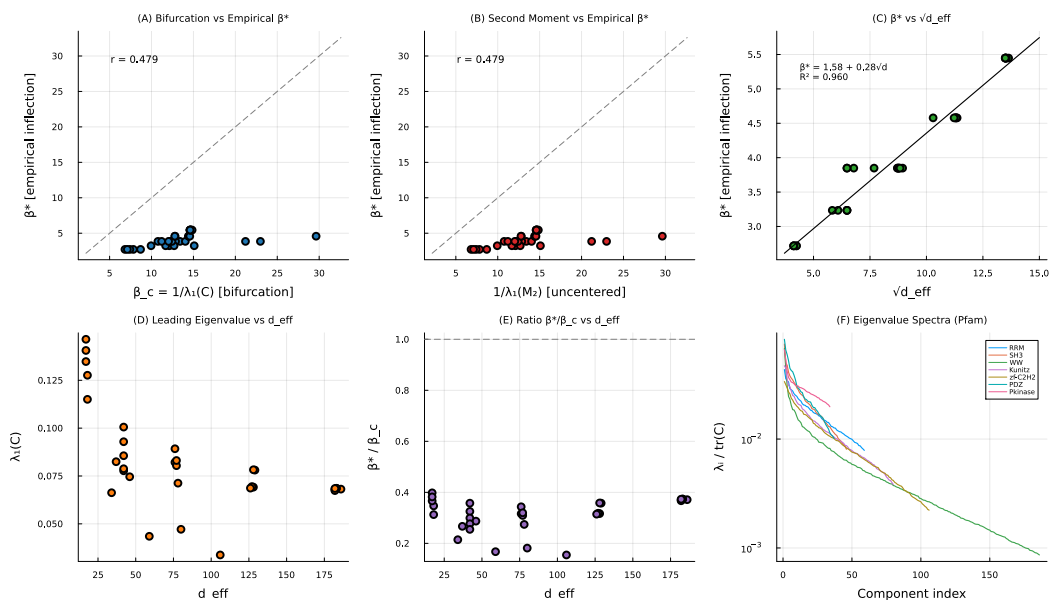


Figure S8: **Stored-pattern probe analysis.** (A) Validation:  $\beta^*$  recomputed from stored-pattern inflection vs. the value from find\_entropy\_inflection ( $R^2 = 0.924$ ). (B) Cross-similarity variance (stored probes) vs. random-probe variance ( $1/d$ ); stored probes systematically deviate from the identity line. (C) Variance ratio  $\sigma^2_{cross}/\sigma^2_{random}$  vs.  $d$ ; no consistent relationship. (D) The decomposition  $\tau^*_{stored}/\sigma_{cross}$  fails as a predictor of  $\beta^*$  ( $R^2 = -9.0$ ). (E) Self-similarity gap  $\Delta = 1 - \max_{j \neq k} \mathbf{m}_j^T \mathbf{m}_k$  vs.  $d$ . (F)  $\beta^*$  vs.  $1/\Delta$  ( $r = 0.76$ ); the gap has moderate predictive power but is noisier than  $\sqrt{d}$ .



**Figure S9: Bifurcation-based prediction of  $\beta^*$  and eigenvalue spectra.** (A) Bifurcation predictor  $\beta_c = 1/\lambda_1(\mathbf{C})$  vs. empirical  $\beta^*$  ( $r=0.479$ ); the bifurcation point systematically overshoots  $\beta^*$  by a factor of 3–5 and has poor predictive power. (B) Second-moment predictor  $1/\lambda_1(\mathbf{M}_2)$  vs. empirical  $\beta^*$  ( $r=0.479$ ); performance is identical to the bifurcation predictor, confirming that the leading eigenvalue does not capture the relevant transition scale. (C)  $\beta^*$  vs.  $\sqrt{d_{\text{eff}}}$  with fitted model  $\beta^* = 1.58 + 0.28\sqrt{d}$  ( $R^2=0.960$ ); PCA dimensionality is the effective predictor. (D) Leading eigenvalue  $\lambda_1(\mathbf{C})$  vs.  $d_{\text{eff}}$ ; no consistent relationship. (E) Ratio  $\beta^*/\beta_c$  vs.  $d_{\text{eff}}$ ; the ratio is consistently 0.2–0.4, well below the naive bifurcation prediction (dashed line at 1.0), confirming that bifurcation systematically overestimates  $\beta^*$ . (F) Normalized eigenvalue spectra  $\lambda_i/\text{tr}(\mathbf{C})$  for all eight Pfam families on a log scale; spectra decay rapidly after the leading components, motivating the PCA variance-threshold dimension as the relevant scale.